# UC Irvine

## UC Irvine Previously Published Works


### Title

Distinct dynamics and intrinsic properties in ventral tegmental area populations mediate reward association and motivation.


### Permalink

https://escholarship.org/uc/item/9qm5810b



### Journal

Cell Reports, 43(9)



### Authors

Elum, Jordan

Szelenyi, Eric

Juarez, Barbara

et al.



### Publication Date

2024-09-24

### DOI

10.1016/j.celrep.2024.114668

Peer reviewed



eScholarship.org Powered by the California Digital Library
University of California

Author Manuscript

Author Manuscript

Author Manuscript

Author Manuscript

HHS Public Access

Author manuscript

*Cell Rep*. Author manuscript; available in PMC 2024 October 28.

Published in final edited form as:

*Cell Rep*. 2024 September 24; 43(9): 114668. doi:10.1016/j.celrep.2024.114668.

# Distinct dynamics and intrinsic properties in ventral tegmental area populations mediate reward association and motivation

**Jordan E. Elum**[1], **Eric R. Szelenyi**[2,9], **Barbara Juarez**[3], **Alexandria D. Murry**[2], **Grigory Loginov**[4], **Catalina A. Zamorano**[5,9], **Pan Gao**[6], **Ginny Wu**[6], **Scott Ng-Evans**[7], **Joshua X. Yee**[8], **Xiangmin Xu**[6], **Sam A. Golden**[1,2,9], **Larry S. Zweifel**[1,5,7,9,10,*]

[1]Graduate Program in Neuroscience, University of Washington, Seattle, WA, USA

[2]Department of Biological Structure, University of Washington, Seattle, WA, USA

[3]Department of Neurobiology, University of Maryland, Baltimore, MD, USA

[4]Center for Integrative Brain Research, Seattle Children's Research Institute, Seattle, WA, USA

[5]Department of Pharmacology, University of Washington, Seattle, WA, USA

[6]Department of Anatomy and Neurobiology, School of Medicine, University of California, Irvine, Irvine, CA, USA

[7]Department of Psychiatry and Behavioral Sciences, University of Washington, Seattle, WA, USA

[8]Vaccine and Infectious Disease Division, Fred Hutchinson Cancer Center, Seattle, WA, USA

[9]University of Washington Center of Excellence in Neurobiology of Addiction, Pain, and Emotion (NAPE), Seattle, WA, USA

[10]Lead contact

## SUMMARY

Ventral tegmental area (VTA) dopamine neurons regulate reward-related associative learning and reward-driven motivated behaviors, but how these processes are coordinated by distinct VTA neuronal subpopulations remains unresolved. Here, we compare the contribution of two primarily dopaminergic and largely non-overlapping VTA subpopulations, all VTA dopamine neurons and VTA GABAergic neurons of the mouse midbrain, to these processes. We find that the dopamine subpopulation that projects to the nucleus accumbens (NAc) core preferentially encodes reward-

*Correspondence: larryz@uw.edu.

AUTHOR CONTRIBUTIONS

J.E.E. and L.S.Z. conceptualized the project and experimental design for all experiments. J.E.E. and C.A.Z. collected the fiber photometry datasets. J.E.E. and G.L. collected the optogenetics datasets. B.J. designed, collected, and analyzed the electrophysiology datasets. J.E.E., E.R.S., A.D.M., and S.A.G. designed, collected, and analyzed the monosynaptic input mapping datasets. P.G., G.W., and X.X. provided the helper and rabies viruses and assisted with input mapping validation experiments. S.N.-E. wrote all MedAssociates scripts and designed and built custom operant chamber equipment and digital and analog electronics. J.E.E. wrote Python, MATLAB, and R scripts and analyzed all the other datasets. J.X.Y. wrote Python scripts. G.L., S.N.-E., and L.S.Z. assisted with additional data analyses. J.E.E., B.J., E.R.S., and L.S.Z wrote the manuscript, and all authors reviewed the manuscript.

DECLARATION OF INTERESTS

The authors declare no competing interests.

SUPPLEMENTAL INFORMATION

Supplemental information can be found online at https://doi.org/10.1016/j.celrep.2024.114668.

Author Manuscript Author Manuscript Author Manuscript Author Manuscript

predictive cues and prediction errors. In contrast, the subpopulation that projects to the NAc shell preferentially encodes goal-directed actions and relative reward anticipation. VTA GABA neuron activity strongly contrasts VTA dopamine population activity and preferentially encodes reward outcome and retrieval. Electrophysiology, targeted optogenetics, and whole-brain input mapping reveal multiple convergent sources that contribute to the heterogeneity among VTA dopamine subpopulations that likely underlies their distinct encoding of reward-related associations and motivation that defines their functions in these contexts.

## In brief

Elum et al. demonstrate that subpopulations of dopamine neurons and GABA neurons of the ventral tegmental area differentially encode task-specific variables during reinforcement learning and motivation. They further demonstrate that the distinct functions of dopamine subpopulations and their encoding of reward-related information are related to differences in intrinsic excitability and connectivity.

## Graphical abstract

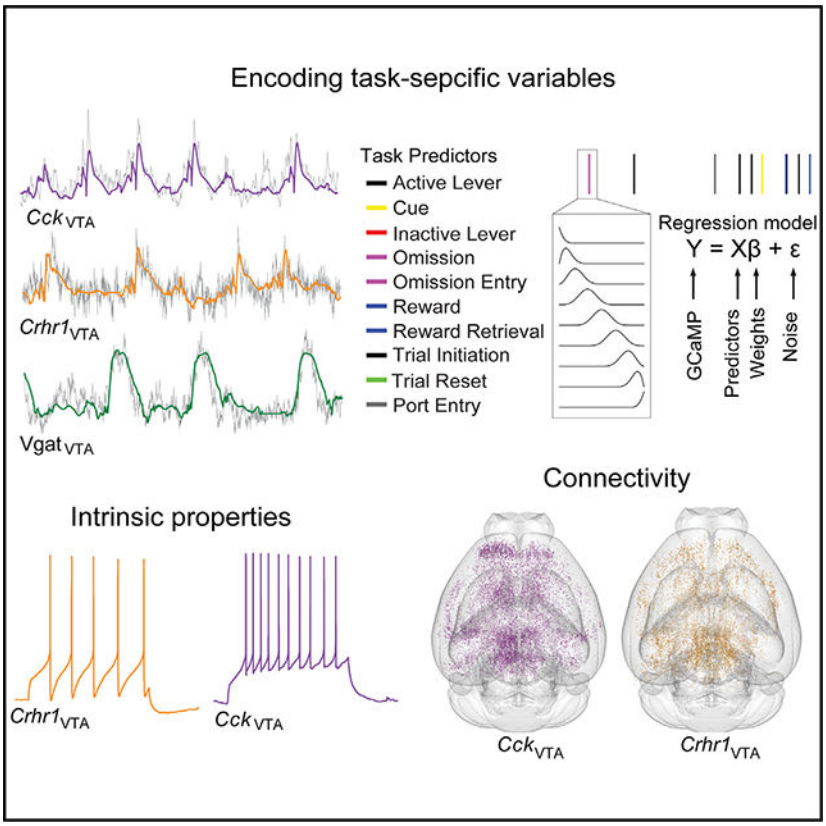


## INTRODUCTION

Classical models of learning and motivational processes implicate a role for mesolimbic dopamine in multiple facets of reinforcement learning and motivation. Phasic dopamine neuron activity encodes prediction error signals, which support value-based learning

Author Manuscript Author Manuscript Author Manuscript Author Manuscript

processes.[1,2] Mesolimbic dopamine also provides an incentive salience signal to modulate the strength and persistence of motivated responding.[3–6] When animals behave in complex tasks and naturalistic environments, dopamine neurons display heterogeneous and multiplexed responses.[2,7–26] Consistent with this pattern of heterogeneity in regulating diverse behavioral functions, ventral tegmental area (VTA) dopamine neurons are heterogeneous in their afferent and efferent connectivity and intrinsic electrophysiological properties.[27–30]

To better understand how heterogeneity in the mesolimbic dopamine system contributes to motivated behavior, recent studies have emphasized the role of local control of dopamine release via postsynaptic mechanisms in the striatum for the motivational functions of VTA dopamine.[31] Others have focused on projection-specific dopamine populations and demonstrated that different regions of the striatum receive distinct dopamine signals.[11,32–34] They have further shown that distinct mesolimbic dopamine pathways encode value and prediction error information.[35] Recent work has identified differential functional roles for dopamine projections to the nucleus accumbens (NAc) core and NAc shell in mediating Pavlovian association[30,36] and appetitive and aversive motivation, respectively.[30,37] These findings and others have been integrated into an updated model in which, rather than uniformly reflecting homogeneous teaching and motivation signals, heterogeneous midbrain dopamine neurons have nuanced roles in reward-related learning and motivated behaviors.[38]

The VTA contains multiple types of neurons including dopaminergic, GABAergic, glutamatergic, and combinatorial populations, many of which co-release neurotransmitters and neuropeptides.[28,39–41] Importantly, VTA GABA neurons comprise roughly one-third of all VTA neurons,[39] regulate VTA dopamine neuron excitability through direct inhibition,[42–46] mediate ongoing motivated behavior,[46] and modulate VTA dopamine neuron prediction error responses.[47] Monosynaptic tracing studies have revealed that VTA neurons receive inputs from a diverse array of brain regions,[27,48–51] many of which carry mixed information related to reward prediction.[51] Among the numerous inputs to the VTA, many are inhibitory and synapse onto VTA GABAergic neurons,[44] resulting in disinhibition of VTA dopamine neurons.[42,43,52,53] Although VTA GABA neurons have been implicated in motivated behavior, integrating these findings with an updated understanding of heterogeneous projection-defined dopamine populations has presented a challenge. Here, we use fiber photometry and optogenetics during behavior to examine the neural correlates and functional significance of VTA dopamine populations and the VTA GABAergic population in reward-related associative learning and reward-driven motivational processes. Furthermore, we use electrophysiology, targeted optogenetics, and whole-brain input mapping to further resolve relationships between the activity dynamics during behavior and intrinsic neurophysiological and circuit properties of these cells.

## RESULTS

### VTA subpopulations display distinct response profiles during instrumental conditioning

To resolve the encoding task-related features in dopamine subpopulations, we monitored activity-related calcium signals in dopamine neurons that have been shown to differentially innervate the NAc core (*Crhr1*$_{VTA}$ cells) or NAc shell (*Cck*$_{VTA}$ cells)[30] during a cued

Author Manuscript Author Manuscript Author Manuscript Author Manuscript

reinstatement paradigm[54,55] (Figures 1A and 1B). We also monitored neural activity dynamics in VTA dopamine neurons as a whole ($DAT_{VTA}$) and in VTA GABAergic neurons ($Vgat_{VTA}$). *Slc6a3*(DAT)-*Cre*, *Cck*-Cre, *Crhr1*-Cre, and *Slc32a1*(Vgat)-Cre mice were injected with an adeno-associated virus (AAV) expressing a Cre-dependent GCaMP6m in the VTA and implanted with an optical fiber above the VTA for fiber photometry recording of time-varying bulk GCaMP fluorescence (Figures 1C–1O, and S1A–S1C). Analysis of calcium transients during baseline recording revealed significant differences among the populations (Figures S2A–S2D).

During acquisition, GCaMP fluorescence was elevated following reward delivery in all four populations, although the latency to peak following reward delivery was greater in the $Vgat_{VTA}$ population (Figures 1C–1O and 1P). Interestingly, the $Vgat_{VTA}$ populations also displayed prolonged activity after reward delivery (Figures 1M–1O). Dopamine populations showed increased activity during the trial initiation press and conditioned stimulus (CS) presentation periods that was significantly different from the pretrial initiation (Pre-LP) period (Figures 1D–1L). GCaMP fluorescence in $Vgat_{VTA}$ neurons during the action and cue periods was not significantly different from the pretrial initiation period (Figures 1M–1O). While both dopamine subpopulations showed phasic responses to these task events, the $Cck_{VTA}$ population showed a sustained elevation of GCaMP fluorescence during the full action cue-outcome period following trial initiation that was significantly different from the $Crhr1_{VTA}$ population (Figures 1G–1I and S2E). In addition, we found that $Cck_{VTA}$ population activity increased several seconds before mice initiated a trial early in training (Figure S2F). By contrast, the $Crhr1_{VTA}$ population showed a decrease in activity prior to trial initiation early in training (Figure S2F). During extinction, dopamine populations showed modest responses to the lever-press and port-entry bout onsets, while $Vgat_{VTA}$ showed a phasic activation during unrewarded port-entry bout onset (Figures 1D–1O and 1R). During reinstatement, dopamine populations responded to non-contingent presentations of the cue, but the $Vgat_{VTA}$ population did not (Figures 1D–1O, 1S, and 1T). During the contingent phase of reinstatement, dopamine populations showed increased fluorescence to the action and cue responses similar to their response profiles to these periods during acquisition (Figures 1D–1L). $Vgat_{VTA}$ neurons showed a sustained decrease in activity during the action and cue periods in contrast to their activity profile during acquisition (Figures 1M–1O). Again, during the trial outcome period, the $Cck_{VTA}$ population showed a greater latency to decay following omission compared to the $Crhr1_{VTA}$ population (Figures 1U and 1V).

## Differential contribution of dopamine subpopulations to cued reinstatement of reward-seeking behavior

We find that both $Cck_{VTA}$ and $Crhr1_{VTA}$ neurons are active during cued reinstatement, and it has been shown that activation of dopamine neurons is sufficient to reactivate a previously extinguished behavior.[56–58] Whether either or both $Cck_{VTA}$ and $Crhr1_{VTA}$ neurons mediate the reactivation of cue-driven instrumental responding following extinction remains unclear. To address this, we photostimulated both populations during CS presentation throughout the reinstatement session. *Cck*-Cre and *Crhr1*-Cre mice were injected with an AAV expressing a Cre-dependent ChR2 or GFP in the VTA and implanted with an optical fiber above the VTA

Author Manuscript Author Manuscript Author Manuscript Author Manuscript

(Figures 2A and S3A–S3B). Mice were trained on the acquisition and extinction phases of the cued reinstatement task without photostimulation (Figures 2B, 2C, S3C, and S3D). To rule out the possible confound of reinforcement of lever pressing by photostimulation in the absence of CS presentation, we photostimulated each population for 3 s (20 Hz, 5-ms pulse width, 3-s duration) following an active lever press during an additional extinction session (Stim) prior to the reinstatement session (Stim + CS) (Figure 2B). Photostimulation of either population 3 s following an active lever press in the absence of CS presentation did not affect operant responding (Figure 2D). We next asked whether photostimulation of these neurons during CS presentation is sufficient to alter rein-statement behavior (Stim + CS) (Figure 2B). CS presentation paired with photostimulation of *Crhr1*$_{VTA}$, but not *Cck*$_{VTA}$, neurons during cued reinstatement significantly increased the number of active lever presses during the entire session (Figures 2D and 2E) but did not alter the total number of trials completed (Figure 2F) or the number of inactive lever presses (Figure S3E).

To determine if the activity observed in dopamine subpopulations during CS presentation causally contributes to cued rein-statement behavior, we photoinhibited both populations during CS presentation throughout the reinstatement session (Figure 2H). *Cck*-Cre and *Crhr1*-Cre mice were injected bilaterally with an AAV carrying Cre-dependent inhibitory JAWS or GFP in the VTA and implanted with bilateral optical fibers above the VTA (Figures 2G and S3F–S3G). Mice performed the acquisition and extinction phases of the cued reinstatement task without photoinhibition (Figures 2H, 2I, and S3H–S3J). VTA subpopulations were photoinhibited for 3 s (2-s constant square pulse terminated with a 1-s linear ramp down to avoid rebound excitation[24]) during the CS presentation throughout the cued reinstatement session (Light + CS) (Figure 2H). Photoinhibition of *Crhr1*$_{VTA}$, but not *Cck*$_{VTA}$, neurons reduced the total number of lever presses in the reinstatement session (Light + CS) (Figures 2J and 2K) and the total number of trials completed (Figure 2L). Photoinhibition did not alter the number of inactive lever presses (Figure S3J). Taken together, these findings indicate that the contribution of *Crhr1*$_{VTA}$ neurons to cued reinstatement is distinct from that of *Cck*$_{VTA}$ neurons.

## Differential encoding of prediction error and behavioral variables by VTA subpopulations

Dopamine neurons encode reward prediction errors,[1] and it has been reported that this is a uniform feature of these cells.[59] To test whether dopamine subpopulations uniformly encode prediction errors, we recorded GCaMP fluorescence while mice performed a modified version of the acquisition task in which we introduced random unpredictable reward omissions and reduced the overall reward probability following cue presentation to 50% (Figures 3A and 3B). Mice showed a significantly shorter latency to initiate a new trial following an unrewarded trial compared to rewarded trials (Figure 3C). VTA dopamine populations and the Vgat$_{VTA}$ population showed different responses to reward and omission trials, with greater activity following sucrose reward (Figures 3D–3K). The VTA dopamine populations show an increase in GCaMP fluorescence following rewarded trial port entries and a decrease in fluorescence following unrewarded port entries (Figures 3D–3I). However, latency to the minimum GCaMP response following unrewarded trial port entry was significantly shorter in the *Crhr1*$_{VTA}$ population relative to the *Cck*$_{VTA}$ population (Figures S4A and S4B). Additionally, the increase in GCaMP fluorescence following port entry in

Author Manuscript Author Manuscript Author Manuscript Author Manuscript

rewarded trials was greater in the $Cck_{VTA}$ neurons relative to the $Crhr1_{VTA}$ neurons (Figures S4C and S4D). In contrast, the $Vgat_{VTA}$ population shows an increase in fluorescence following both rewarded and unrewarded trial outcomes (Figures 3J and 3K), consistent with its role in modulating reward prediction in VTA dopamine neurons.[47]

To compare expectation-dependent modulation of reward outcome responses among VTA subpopulations,[1] we examined how GCaMP fluorescence correlated with rewarded and unrewarded trial outcomes according to the type of outcome on the preceding trial (Figures 3L–3O and S4E–S4H). In $DAT_{VTA}$ and $Crhr1_{VTA}$ populations, we observed greater reductions in the GCaMP signal when a reward omission trial was preceded by a rewarded trial compared to an unrewarded trial (Figures 3L and 3N). However, we did not observe a change in reward omission response between previous trial outcome conditions in $Cck_{VTA}$ neurons (Figure 3M). Responses to reward omissions in $Vgat_{VTA}$ neurons were also unaffected by the previous trial outcome (Figure 3O). We found that $Cck_{VTA}$ and $Vgat_{VTA}$ populations showed greater increases in GCaMP fluorescence when a rewarded trial was preceded by an unrewarded trial compared to a rewarded trial (Figures S4F–S4H).

Next, we fit a linear regression model to predict VTA population trial outcome activity using the current and previous five trial outcome identities as predictors (Figure 3P; adapted from Bayer and Glimcher[60]). All dopamine populations showed a decay in the influence of previous trial outcomes on their activity (Figures 3Q–3S). However, only the $DAT_{VTA}$ and $Crhr1_{VTA}$ populations showed the distinctive combination of a positive modulation by the current trial outcome and a negative modulation by the previous trial outcome (Figures 3Q and 3S). This result suggests that the $Cck_{VTA}$ population preferentially reflects information about current trials, whereas the $Crhr1_{VTA}$ neurons are modulated by reward history. Thus, although both dopamine subpopulations have reward prediction error (RPE)-like signals during reward omission, they show differential retrospective modulation of these responses.

Finally, we compared the relative contribution of task events (lever press, cues, outcomes, port entry) and focused our analysis on the $Cck_{VTA}$ and $Crhr1_{VTA}$ dopamine subpopulations and the $Vgat_{VTA}$ GABAergic population. To this end, we fit the GCaMP signal of each mouse with a linear encoding model (Figures 4A and 4B; adapted from Engelhard et al.[7] and Parker et al.[61]). To characterize the relative contribution of different task event types in predicting GCaMP fluorescence, we quantified the decrease in explained variance when a given task predictor variable was excluded from the encoding model (Figures 4C–4H). We found that the $Cck_{VTA}$ population showed preferential activation to cue and the trial LP (Figure 4D) (Figure 4C), but the $Crhr1_{VTA}$ population showed preferential encoding of the cue relative to the other action cue periods (Figure 4D), and this encoding was significantly different between the populations (Figure 4I). By contrast, none of the task predictor variables had a significantly different relative contribution to neural activity during the action cue period in the $Vgat_{VTA}$ population (Figures 4E, 4I, and 4J). During the trial outcome period, reward contributed most strongly to the predicted response, followed by reward retrieval, in both dopamine subpopulations (Figures 4F and 4G). However, the $Vgat_{VTA}$ population most strongly encoded reward retrieval, followed by reward (Figure 4H), which was significantly different from the $Cck_{VTA}$ and $Crhr1_{VTA}$ dopamine subpopulations (Figures 4K and 4L).

Author Manuscript Author Manuscript Author Manuscript Author Manuscript

## VTA populations differentially encode incentive motivation

VTA dopamine neuron activity is correlated with effort exertion that is thought to invigorate ongoing motivated behaviors.[62,63] To address whether dynamic changes in effort and reward availability are represented across VTA dopamine subpopulations and the VTA GABA population, we recorded GCaMP fluorescence while mice underwent a progressive ratio test. In this task, the number of lever presses to earn a reward is increased systematically throughout the session (Figure 5A) that allows for the measure breakpoint, the maximum effort an animal will exert before stopping.[64] Mice tracked this increasing response requirement, reflected in the high number of cumulative lever press responses across mice (Figures 5B and 5C).

We found that activity in both dopamine subpopulations is transiently increased at the onset of bouts of lever pressing (Figures 5D–5G), with the *Cck*$_{VTA}$ cells showing significantly higher response than the *Crhr1*VTA or Vgat$_{VTA}$ populations (Figure S4I). During unrewarded port entry bout onset, all VTA populations showed a small increase in activity prior to bout onset followed by a decrease to baseline during the duration of the bout (Figures 5D–5I), with the *Crhr1*$_{VTA}$ neurons displaying a decrease below baseline that was significantly different from the Vgat$_{VTA}$ population with *Cck*$_{VTA}$ neurons displaying an intermediated response (Figure S4J). During rewarded port entries, activity in both dopamine subpopulations ramped up prior to reward retrieval and showed sustained activity during reward consumption (Figures 5D–5G), with *Cck*$_{VTA}$ neurons showing larger overall responses (Figure S4K). Vgat$_{VTA}$ neurons showed a relatively modest increase in activity prior to reward retrieval, in contrast to VTA dopamine populations (Figures 5H and 5I), but showed sustained activity following retrieval (Figures 5H and 5I).

To determine how the response profiles of VTA subpopulations evolve across increasing effort requirements and decreasing reward availability, we examined neural activity as a function of the breakpoint of each mouse. We found that *Crhr1*$_{VTA}$ and *Cck*$_{VTA}$ populations showed distinct activity profiles in response to decreasing reward availability. *Cck*$_{VTA}$ population activity at lever press bout onset was initially high and sustained during the entire bout earlier in the session with lower lever press response requirements (Figure 5J). However, *Cck*$_{VTA}$ population activity during lever press bout onset was decreased later in the session, as rewards required more effort to obtain them (Figure 5J). By contrast, the *Crhr1*$_{VTA}$ population responded similarly at lever press bout onset regardless of response requirements (Figure 5K). Further, we found that decreased reward availability was associated with less activity in the *Cck*$_{VTA}$ population during lever press bouts across the entire session but not in the *Crhr1*$_{VTA}$ or Vgat$_{VTA}$ population (Figures 5M–5O). A statistical comparison of the correlation between the percentage of breakpoint and GCaMP response during LP bout onset across mice revealed a significant difference between the *Cck*$_{VTA}$ and *Crhr1*$_{VTA}$ populations (Figure 5P).

## Electrophysiological properties and connectivity of Crhr1$_{VTA}$ and Cck$_{VTA}$ populations

To determine whether differences in the response profiles of *Cck*$_{VTA}$ and *Crhr1*$_{VTA}$ neurons are related to differences in their intrinsic electrophysiological properties and/or connectivity, we performed whole-cell, voltage, and current-clamp recordings *ex vivo*. *Cck*-

Author Manuscript Author Manuscript Author Manuscript Author Manuscript

Cre and *Crhr1*-Cre mice were injected with an AAV carrying Cre-dependent EYFP in the VTA to isolate cells (Figure 6A). To examine the intrinsic excitability of $Crhr1_{VTA}$ and $Cck_{VTA}$ subpopulations, we recorded action potential firing from EYFP-labeled cells in response to increasing steps of current injection (Figures 6B–6D). $Cck_{VTA}$ and $Crhr1_{VTA}$ neurons continued to increase firing with increasing current injections (Figure 6C). However, $Cck_{VTA}$ neurons fired a greater number of action potentials in response to depolarizing steps of current and showed a shorter latency to spike following current injection compared to $Crhr1_{VTA}$ neurons (Figures 6C and 6D).

Next, we recorded spontaneous inhibitory postsynaptic currents (sIPSCs) in these two populations (Figure 6E). $Cck_{VTA}$ and $Crhr1_{VTA}$ neurons did not differ in sIPSC frequency (Figure 6F); however, we did observe that $Crhr1_{VTA}$ neurons showed slightly smaller-amplitude sIPSCs compared to $Cck_{VTA}$ neurons (Figure 6G). Finally, we asked if there is a difference in rebound depolarization and spiking following injection of a hyperpolarizing current between $Cck_{VTA}$ and $Crhr1_{VTA}$ neurons. $Cck_{VTA}$ neurons showed a shorter latency to spike and a faster membrane potential rise time following the offset of a hyperpolarizing step compared to $Crhr1_{VTA}$ neurons (Figures 6H–6J). Taken together, these results establish distinct intrinsic properties of $Cck_{VTA}$ and $Crhr1_{VTA}$ neurons, which could contribute to their distinct activity patterns *in vivo*.

Next, we asked whether these cells respond differently to the activation of inhibitory inputs or disinhibitory inputs *in vivo*. Based on prior work,[41,44,46,52,53] we assessed the responsivity of $Cck_{VTA}$ and $Crhr1_{VTA}$ neurons to proximal GABA inputs from within the VTA and distal GABA inputs from outside the VTA, namely lateral hypothalamus (LH) GABA neurons or NAc medial shell (mshell) GABA neurons, while recording calcium dynamics in VTA dopamine subpopulations. For local VTA GABA inputs, we injected *Cck*-Cre *Vgat*-Flp or *Crhr1*-Cre *Vgat*-Flp mice with an AAV carrying Flp-dependent ChrimsonR-tdTomato in $Vgat_{VTA}$ neurons and an AAV carrying Cre-dependent GCaMP6m in either $Cck_{VTA}$ and $Crhr1_{VTA}$ neurons in the VTA and implanted an optic fiber for dual recording and stimulation above the VTA (Figures 6K and S5A). When the $Vgat_{VTA}$ population was stimulated with red light (20 or 40 Hz, 3-s duration), we observed a significant decrease in GCaMP fluorescence relative to the prestimulation period in both $Cck_{VTA}$ and $Crhr1_{VTA}$ populations (Figure 6L). Compared to the $Cck_{VTA}$ population, the $Crhr1_{VTA}$ population showed a larger amplitude inhibitory response at the 40-Hz stimulation (Figure 6M). This is surprising based on the slightly increased amplitude of sIPSCs in $Cck_{VTA}$ neurons compared to $Crhr1_{VTA}$ neurons but may reflect differences in spontaneous calcium transients, increased excitability, and enhanced rebound from hyperpolarization in $Cck_{VTA}$ neurons.

Next, we examined how stimulation of the LH GABA or NAc mshell GABA population impacts the VTA dopamine subpopulations. Using a similar strategy, we expressed Flp-dependent ChrimsonR-tdTomato in either LH GABA neurons or NAc mshell GABA neurons and GCaMP6m in either $Cck_{VTA}$ or $Crhr1_{VTA}$ neurons and implanted an optic fiber for stimulation above the LH or NAc mshell and an optic fiber for recording above the VTA (Figures 6N, 6Q, and S5B–S5E). We found that photostimulation of LH GABA strongly activated both VTA dopamine populations (Figure 6O–6P). In contrast, photostimulation of

Author Manuscript Author Manuscript Author Manuscript Author Manuscript

NAc mshell GABA evoked a sustained activation only in the *Cck*$_{VTA}$ population at both stimulation frequencies (Figures 6R and 6S).

## Mapping brain-wide monosynaptic inputs to VTA dopamine subpopulations

VTA dopamine neurons receive synaptic input from numerous brain regions,[49–51,65,66] and distinct VTA dopamine projection populations are differentially regulated by multiple upstream regions.[27,48] We hypothesized that *Cck*$_{VTA}$ neurons and *Crhr1*$_{VTA}$ neurons receive distinct patterns of monosynaptic input across the whole brain. To test this, we compared the relative density of brain-wide monosynaptic inputs to *Cck*$_{VTA}$ and *Crhr1*$_{VTA}$ populations using rabies virus-based transsynaptic retrograde tracing[67] paired with tissue clearing and light sheet fluorescence microscopy (LSFM). AAV-*syn*-DIO-TC66T-2A-EGFP-2A-oG was injected into the VTA of *Cck*-Cre or *Crhr1*-Cre mice, followed by an injection of EnvA-SADΔG-RV-dsRed 14 days later (Figure 7A). After 9 days, intact brains were optically cleared and imaged using LSFM (Figure 7A). Starter cell populations in the VTA were identified based on EGFP and dsRed co-expression (Figure S6A). Transsynaptically labeled neurons were identified based on dsRed-only expression (Figure S6B). To quantify the anatomical distribution of input cells, we used a modified ClearMap pipeline[68,69] for brain atlas registration and automated cell detection. For both *Cck*$_{VTA}$ and *Crhr1*$_{VTA}$ starter cell populations, dsRed-positive input cells were found across the brain (Figures 7B–7D, S6B, S6D, and S7A–S7C). While the total number of input cells varied across mice, the number of starter cells and input cells was roughly proportional (Figure S6E). Cell counts across all brain regions were normalized to the total number of input cells for each mouse to account for variability in the total number of labeled neurons.

Brain-wide cellular inputs were assessed by mean cell density per voxel (Figure 7C, first and third images) to identify group differences (Figure 7C, second and fourth images). An orthogonal analysis was also conducted on brain-atlas-segmented counts, with group mean statistical comparisons made on a region-by-region basis (Figures 7D and 7E). We found significant differences in input density from multiple regions in the striatum, pallidum, amygdala, hippocampus, hypothalamus, midbrain, and hindbrain (Figures 7C–7E; Table S1). *Cck*$_{VTA}$ neurons had greater reciprocal connections with their NAc projection target (Figures 7C–7E). In pallidal areas, the ventral pallidum was primarily a source of *Cck*$_{VTA}$ neurons, whereas the dorsal globus pallidus contained inputs preferentially to *Crhr1*$_{VTA}$ neurons (Figures 7C–7E). The central amygdala predominantly contained *Crhr1*$_{VTA}$ input neurons, whereas the hippocampus connected predominantly to *Cck*$_{VTA}$ neurons (Figures 7C–7E). A variety of septal regions (including the medial septal nucleus [MSN] and diagonal band) and hypothalamic regions (including the medial preoptic and lateral preoptic areas, LH, and posterior hypothalamic nuclei) contained significantly more *Cck*$_{VTA}$ input neurons (Figures 7C–7E). *Crhr1*$_{VTA}$ neurons received significantly more input from zona incerta and multiple midbrain and hindbrain regions (e.g., medial reticular formation, superior colliculus [SC], periaqueductal gray [PAG], substantia nigra pars reticular part, pontine reticular nucleus, and cuneiform nucleus) (Figures 7C–7E). Clustered brain-wide input differences between *Cck*$_{VTA}$ and *Crhr1*$_{VTA}$ neurons into canonical functional networks based on the designation of Xu and colleagues[70] (Figure 7E; see STAR Methods) revealed that *Cck*$_{VTA}$ neurons received preferential inputs from regions involved in motivation and action selection

Author Manuscript Author Manuscript Author Manuscript Author Manuscript

(Figure 7E), whereas *Crhr1*$_{VTA}$ neurons received preferential inputs from regions involved in sensory-motor integration and affect (Figure 7E).

## DISCUSSION

### Distinct functions of activity in VTA subpopulations for reward association and motivation

Here, we found that the response profiles of projection-defined dopamine populations are broadly similar during a cued reinstatement task. This is consistent with existing evidence that dopamine neurons respond relatively uniformly (similar response profile to action, cue, and outcomes) during simple instrumental conditioning tasks.[7,30,71] We observed patterns of sustained activity on long timescales (10-s) prior to reward delivery preferentially in the *Cck*$_{VTA}$ population. Gradual increases in dopamine neuron activity and dopamine release as animals perform goal-directed behaviors and approach rewards has been reported.[30,31,72–75] The sustained increase in activity we observed in the *Cck*$_{VTA}$ population during the action cue period prior to reward across acquisition sessions could reflect a reward anticipation signal or an overall increased level of motivational engagement at trial onset.

When reward probability or reward effort was varied, we found heterogeneous responses with non-uniform encoding of prediction error, behavioral variables, and reward anticipation across NAc core and NAc shell-projecting subpopulations. During random reward omission, *Crhr1*$_{VTA}$ activity reflected a prediction-error-like signal, while *Cck*$_{VTA}$ activity reflected a salience signal. The observed positive modulation of dopamine neuron activity by current trial outcome and negative modulation by previous trial outcome support the notion that *Crhr1*$_{VTA}$ neurons are more involved in prediction error encoding compared to *Cck*$_{VTA}$ neurons. By contrast, the *Cck*$_{VTA}$ population preferentially encoded the trial initiation lever press action compared to the non-trial active lever press action. Taken together, these results suggests that *Crhr1*$_{VTA}$ neurons strongly encode reward-associated stimuli and integrate predictive information over time to drive future behavior, whereas *Cck*$_{VTA}$ neurons strongly encode goal-directed actions and provide a salience signal to drive ongoing behavior.

Previous studies showed that VTA dopamine activity is negatively correlated with effort and reward attainability.[62,73] Our observations demonstrate that this is not uniform across dopamine populations and was only observed in the *Cck*$_{VTA}$ population, consistent with these neurons regulating incentive motivation.[30] Together, these findings suggest that modulation of prediction-error-encoding based on prior outcomes, action cue encoding, and incentive motivation encoding involve dopamine populations with distinct projections to the NAc. In contrast to previous studies,[31] our results suggest that sustained cell body activity in a distinct subpopulation of VTA dopamine neurons during behavior contributes to ongoing motivated responding. Further, consistent with our observed pattern of functional heterogeneity across VTA dopamine subpopulations, it was recently demonstrated that dopamine neurons in the medial VTA display sustained activity patterns during behavior and encode behavioral state, whereas anatomically distinct lateral VTA dopamine neurons display transient activity and encode behavioral rate of change.[35]

While dopamine populations showed transient and sustained responses during instrumental responses and cues, the Vgat$_{VTA}$ population responded selectively during reward outcome

Author Manuscript Author Manuscript Author Manuscript Author Manuscript

periods. When reward was available, $Vgat_{VTA}$ responses were sustained throughout reward consumption. Unrewarded port entries, however, evoked smaller, brief increases in $Vgat_{VTA}$ activity. Further, the $Vgat_{VTA}$ population preferentially encoded rewarded port entry compared to unrewarded port entry but showed no preferential encoding of behavioral variables during the action cue period. This reward-outcome-dependent difference in activity is consistent with findings that $Vgat_{VTA}$ neurons causally contribute to reward-expectation-driven decreases in VTA dopamine neuron activity.[47] Taken together, these results suggest that VTA GABA neurons reflect reward outcome information and may suppress VTA dopamine activity during reward consumption.

## Heterogeneous intrinsic and circuit properties define distinct VTA dopamine subpopulations

Consistent with the differences we observed in baseline neural activity during periods of task-related behavioral inactivity between $Cck_{VTA}$ and $Crhr1_{VTA}$ populations, our *ex vivo* electrophysiological results revealed that these dopamine subpopulations displayed distinct intrinsic properties that may regulate their endogenous activity. Specifically, the increased baseline excitability of $Cck_{VTA}$ neurons could contribute to their sustained increase in activity observed during multiple behaviors and increased baseline calcium transient width and amplitude. Additionally, we observed a greater level of spontaneous postsynaptic inhibitory transmission in $Cck_{VTA}$ neurons. The amplitude of sIPSCs is correlated with the strength of inhibitory synapses onto the postsynaptic neurons.[76,77] This could be due to multiple mechanisms, including differences in the number, location, or subunit composition of GABA receptors.[78,79]

Previous input mapping studies have revealed that VTA dopamine and VTA GABA neurons receive inhibitory input from many of the same brain regions, including the LH, NAc, PAG, and DRN.[50,53] Recent studies have shown that specific GABAergic projections from the LH and NAc are important for behavioral activation and motivation, respectively.[27,44,52,53,80] Interestingly, our functional optogenetic experiments revealed that NAc shell GABA activation disinhibits $Cck_{VTA}$ neurons selectively. This dedicated NAc shell GABA-VTA GABA-$Cck_{VTA}$ dopamine disinhibitory pathway could provide a mechanism by which information about motivational salience reflected in NAc shell MSN activity drives activity in $Cck_{VTA}$ neurons during goal-directed actions.

Consistent with previous input mapping studies of VTA dopamine neurons, we identified ~100 brain regions connected to $Crhr1_{VTA}$ and $Cck_{VTA}$ neurons, the majority of which were common to both cell types. Interestingly, $Crhr1_{VTA}$ neurons receive a preferential density of inputs from brain regions involved in sensory-motor integration, including the dorsal striatum, globus pallidus, zona incerta, and superior colliculus. By contrast, $Cck_{VTA}$ neurons receive a higher density of inputs from brain regions linked to motivation and action, including the NAc shell, ventral pallidum, and LH.

## Limitations of the study

Although $Cck_{VTA}$ and $Crhr1_{VTA}$ populations are predominantly dopaminergic (~87%), they are not exclusively dopamine releasing and display approximately 25% overlap with each

Author Manuscript Author Manuscript Author Manuscript Author Manuscript

other.[30] These cells also project to other regions, predominantly the amygdala.[30] Thus, the differential encoding observed by these cells may not exclusively reflect their projections to the NAc. Another limitation of this study is the method of normalization of the GCaMP signals. Because of the difference in the number of cells expressing GCaMP across the four VTA populations (Figure S1C) and the differences in the baseline calcium dynamics (Figure S2A), all photometry signals were normalized to the session averages. This approach reduces overall variability and allows for clearer regression analyses (e.g., Figures 3 and 4) and assessment of signal decay and ramping (e.g., Figures 1U, 1V, and S2F). One caveat to this approach is that it can reduce the ability to detect signal amplitude differences across groups that may reflect differences in the genetic underpinnings that contribute to signal variability.[81]

## STAR★METHODS

### RESOURCE AVAILABILITY

**Lead contact—**Further information and requests for resources and reagents should be directed to and will be fulfilled by the lead contact, Larry Zweifel (larryz@uw.edu).

**Materials availability—**All unique stable reagents generated in this study will be made available upon request but may require a payment and/or Material Transfer Agreement if there is a potential for commercial application.

**Data and code availability—**Section 1: Data

- All data reported in this paper will be shared by the lead contact upon request.

Section 2: Code

- All original code has been deposited at Github and is publicly available as of the date of publication. DOIs are listed in the key resources table.

Section 3

- Any additional information required to reanalyze the data reported in this paper is available from the lead contact upon request.

### EXPERIMENTAL MODEL AND STUDY PARTICIPANT DETAILS

Male and female mice, housed on a 12-h light/dark cycle, were used in all experiments performed during the light phase. All procedures were approved and performed under the guidelines of the Institutional Animal Care and Use Committee at the University of Washington (PROTO201600703 – 4249-01). Mice between the ages of 2–6 months were used for all experiments. Vgat-Cre (*Slc32a1*$^{tm2(cre)Lowl}$/J), DAT-Cre (B6.SJL-*Slc6a3*$^{tm1.1(cre)Bkmn}$/J), and *Cck*-Cre (*Cck*$^{tm1.1(cre)Zjh}$/J) were purchased from The Jackson Laboratory and bred in house. *Crhr1*-Cre mice were generated as previously described.[86]

### METHOD DETAILS

**Cued reinstatement task—**Mice were food-restricted to 85%–90% of their *ad libitum* weight and trained on a cued reinstatement task[54,55] in Med Associates operant chambers

Author Manuscript Author Manuscript Author Manuscript Author Manuscript

with two retractable levers and a food port. During 1–2 pre-training sessions, mice were trained to press either lever for immediate delivery of a 20 mg sucrose pellet (Bio-Serv, F0071). All trials were followed by 3-s inter-trial interval. When mice earned 20 pellets within an hour of training, the session ended. In the acquisition task, mice were trained to press the active lever which initiated a 3-s delay period followed by a 3-s cue period (active lever cue light and 2.9 kHz continuous tone). At the end of the cue period, a sucrose pellet was delivered into the food port. At the cue period onset, the box house light was extinguished until the end of the 12.5-s inter-trial interval period. In the extinction task, mice were free to press either lever but all cues and rewards were omitted. In the reinstatement task, 5 non-contingent cue presentations were delivered every 2 min for 10-min during a pre-session period in which the levers were not extended into the box. The pre-session was immediately followed by a 1-h session identical to the acquisition phase except without delivery of food reinforcers.

**Random reward-omission task—**In the random reward-omission task, an active lever press initiated a 3-s delay period followed by a 3-s cue period (active lever cue light and 2.9 kHz continuous tone). Then, at cue offset mice received a food reward on ~50% of trials. Rewarded and unrewarded trials were randomly interspersed throughout the session so that upcoming trial outcomes were unpredictable. At the cue period onset, the box house light was extinguished until the end of the 12.5-s inter-trial interval period regardless of trial outcome type.

**Progressive ratio task—**Food-restricted mice were trained on a fixed-ratio (FR1) schedule of reinforcement for food reward during three daily 1 h sessions in which each active lever press resulted in delivery of a sucrose pellet after a 3-s delay. Then, mice underwent a single session with a progressive ratio schedule of reinforcement in which the number of active lever presses required for each food reinforcer is increased after the completion of each ratio (i.e., 1, 2, 4, 6, 9, 13 …) following a pseudo-exponential function. If no lever press responses were made within a 3-m time period or 120-m elapsed, the session ended.

**Surgery—**Mice (6–8 weeks) were anesthetized with isoflurane (1.5–4%) and head-fixed for stereotaxic (David Kopf Instruments) survival surgery. Stereotactic coordinates were standardized relative to bregma and Lambda distance and an injection syringe was used to inject 0.5 μL of virus at a rate of 0.25 μL/min. Mice recovered from surgery for at least two weeks prior to behavioral testing.

**Fiber photometry—**For fiber photometry behavior experiments, 0.5 μL of AAV1-DIO-GCaMP6m was injected unilaterally into the VTA (A/P: −3.25 mm, M/L: −0.5 mm, D/V: −4.5 mm). Following the virus injection, a fiber optic cannula (400 μm) was implanted 0.5 mm above the VTA.

**Optogenetics—**For photostimulation behavior experiments, 0.5 μL of AAV1-DIO-ChR2-YFP was injected unilaterally into the VTA (A/P: −3.25 mm, M/L: −0.5 mm, D/V: −4.5 mm). Following the virus injection, a fiber optic cannula (200 μm) was implanted 0.5 mm

Author Manuscript Author Manuscript Author Manuscript Author Manuscript

above the VTA. Extinction-resistant mice were excluded from the analysis which resulted in the exclusion of 1 of 17 controls, 1 of 22 *Crhr1*-Cre, and 2 of 18 *Cck-Cre* mice.

For photoinhibition behavior experiments, 0.5 μL of AAV1-DIO-JAWS-GFP was injected bilaterally into the VTA (A/P: −3.25 mm, M/L: ±0.5 mm, D/V: −4.5 mm). Following the virus injection, fiber optic cannulae (200 μm) were implanted 0.5 mm above the VTA bilaterally. The fiber optic cannula was implanted at an angle of 10° on one side. No mice met exclusion criteria for extinction resistance.

For photostimulation and inhibition experiments, control mice were injected with AAV1-DIO-EGFP-KASH.

**Dual optogenetic stimulation and fiber photometry recording—**For dual stimulation and recording experiments of VTA GABA neurons and VTA dopamine subpopulations, 0.5 μL of equal parts AAV1-CAG-FlpX-ChrimsonR-tdTomato and AAV1-DIO-GCaMP6m was injected unilaterally in to the VTA (A/P: −3.25 mm, M/L: −0.5 mm, D/V: −4.5 mm). Following the virus injection, a fiber optic cannula (400 μm) was implanted 0.5 mm above the VTA.

For dual stimulation and recording experiments of LH GABA neurons and VTA dopamine subpopulations, 0.5 μL of AAV1-CAG-FlpX-ChrimsonR-tdTomato was injected unilaterally in to the LH (A/P: −1.35 mm, M/L: −1.0 mm, D/V: −5.0 mm) and AAV1-DIO-GCaMP6m was injected unilaterally in the VTA (A/P: −3.25 mm, M/L: ±0.5 mm, D/V: −4.5 mm). Following the virus injection, a fiber optic cannula (200 μm) was implanted 0.5 mm above the LH at an angle of 5° and a fiber optic cannula (400 μm) was implanted above the VTA.

For dual stimulation and recording experiments of NAc medial shell GABA neurons and VTA dopamine subpopulations, 0.5 μL of AAV1-CAG-FlpX-ChrimsonR-tdTomato was injected unilaterally in to the NAc medial shell (A/P: 1.25 mm, M/L: −0.6 mm, D/V: −4.6 mm) and AAV1-DIO-GCaMP6m was injected unilaterally in the VTA (A/P: −3.25 mm, M/L: ±0.5 mm, D/V: −4.5 mm). Following the virus injection, a fiber optic cannula (200 μm) was implanted 0.5 mm above the NAc medial shell and a fiber optic cannula (400 μm) was implanted above the VTA.

***Ex vivo* slice electrophysiology—**For electrophysiology experiments, 0.5 μL of AAV1-DIO-YFP was injected bilaterally into the VTA (A/P: −3.25 mm, M/L: −0.5 mm, D/V: −4.5 mm).

**Rabies retrograde tracing—**For the retrograde tracing experiment, 0.5 μL of AAV-*syn*-DIO-TC66T-2A-eGFP-2A-oG was injected bilaterally into the VTA (A/P: −3.45 mm, M/L: ±0.5 mm, D/V: −4.5 mm). 14 days later, 0.5 μL of EnvA-SADΔG-RV-DsRed was injected bilaterally into the VTA (A/P: −3.45 mm, M/L: ±0.5 mm, D/V: −4.5 mm).

**Fiber photometry—**GCaMP6m fluorescence was recorded through an implanted optic fiber connected to a patch cord (Doric Lenses) while mice performed behavioral tasks. An LED driver (Doric Lenses) was used to control two LEDs for excitation of GCaMP6m. A 465-nm LED (light intensity: 30–40 μW, sinusoidal frequency modulation: 531 Hz)

Author Manuscript Author Manuscript Author Manuscript Author Manuscript

was used to excite GCaMP6m for calcium-dependent fluorescence. A 405-nm LED (light intensity: 30–40 μW, sinusoidal frequency modulation: 211 Hz) was used to excite GCaMP6m for calcium-independent fluorescence. Light intensity was measured at the optic fiber tip. GCaMP6m fluorescence was collected through the same optic fiber using a photoreceiver (Doric Lenses) and recorded using a Tucker Davis Technologies (TDT) real-time processor (RZ5 BioAmp) at 1017.25 Hz sampling frequency. Task event timestamps were simultaneously registered as TTL pulses by the MedAssociates system and synchronously delivered to the TDT system through a custom interface.

**Fiber photometry preprocessing—**The 405-nm and 465-nm signals were demodulated and downsampled to 50 Hz using a moving average. The downsampled 405-nm control signal was fit to the 465-nm GCaMP6m signal using the 'np.polyfit' function in Python with a degree of 1 to obtain a fitted control signal. The fitted control signal was subtracted from the downsampled 465-nm GCaMP6m signal to correct for calcium-independent fluorescence changes. Then, an exponential curve was fit to the corrected 465-nm signal and subtracted to correct for slow baseline drift due to photobleaching. The baseline-corrected 465-nm GCaMP6m signal for the entire recording session (ΔF/F) was z-scored relative to the mean and standard deviation of the entire session trace to allow for comparison across individual recording sessions and individual mice. The session $Z$ score was defined as ΔF/F(t) mean(ΔF/F(t))/std(ΔF/F(t)). The preprocessed photometry signal was aligned to task events and mean $Z$ score ±SEM was calculated for behavioral epochs of interest. Lever pressing and port entry bouts were classified in either 10-s or 30-s windows aligned to session event times and the first event time per bout (bout onset) was aligned to the photometry signal. Baseline calcium transient analysis was restricted to time periods in which no behavioral event timestamps (lever-press, port entry) were recorded for at least 60-s during the final extinction session of the cued reinstatement task. This resulted in ~20–30-min of baseline recording time per mouse. Transients were identified using the Python 'scipy.signal.find_peaks' function.

**Optogenetics—**For behavioral experiments with optogenetics, mice underwent the pretraining, acquisition, and extinction phases of the cued reinstatement task without laser stimulation. For photostimulation experiments, mice received blue light (3-s, 20 Hz, 5-ms pulse width, ~10 mW light power) unilaterally in the VTA 3-s following active lever press throughout the control stimulation session following the last extinction session. Throughout the cued reinstatement session, mice received blue light (3-s, 20 Hz, 5-ms pulse width, ~10 mW) unilaterally in the VTA during cue presentation. For photoinhibition experiments, mice received red light (2-s constant square pulse terminated with a 1-s linear ramp-down, ~5–10 mW light power) unilaterally in the VTA during cue presentation throughout the cued reinstatement session.

For photostimulation of VTA GABAergic neurons in the VTA, mice were placed in an operant box and received red light (1-s or 3-s, 5–40 Hz, 5-ms pulse width, ~10 mW light power) every 60-s for 80 trials across two sessions. Red light was delivered through the same optic fiber used for fiber photometry recording.

Author Manuscript Author Manuscript Author Manuscript Author Manuscript

For stimulation of LH or Nac medial shell GABAergic neurons, mice received red light (1-s or 3-s, 5–40 Hz, 5-ms pulse width, ~10 mW light power) every 60-s for 80 trials across two sessions. Red light was delivered through an optic fiber above the LH or Nac medial shell.

***Ex vivo* electrophysiology—**Horizontal VTA sections (200 μm) were prepared in an NMDG cutting solution (92 NMDG mM, 2.5 KCl mM, 1.25 $NaH_2PO_4$ mM, 30 $NaHCO_3$ mM, 20 HEPES mM, 25 glucose mM, 2 thiourea mM, 5 Na-ascorbate mM, 3 Na-pyruvate mM, 0.5 $CaCl_2$ mM, 10 $MgSO_4$ mM, pH 7.3–7.4). Then, sections were incubated for ~12 min in the same solution at 32°C in a water bath. Slices were then transferred to a HEPES-aCSF solution (92 NaCl mM, 2.5 KCl mM, 1.25 mM $NaH_2PO_4$ mM, 30 $NaHCO_3$ mM, 20 HEPES mM, 25 glucose mM, 2 thiourea mM, 5 Na-ascorbate mM, 3 Na-pyruvate mM, 2 $CaCl_2$ mM, 2 $MgSO_4$ mM) at room temperature. Slices recovered for an additional 60 min.

Whole-cell, patch-clamp recordings were acquired using the Axopatch 700B amplifier (Molecular Devices) at a sampling frequency of 10 kHz and filtering at 1 kHz eYFP-positive cells were visualized using fluorescence for recording with electrodes at 3–5 MΩ. Excitability recordings were made in an aCSF solution (126 NaCl mM, 2.5 KCl mM, 1.2 $NaH_2PO_4$ mM, 1.2 $MgCl_2$ mM, 11 D-glucose mM, 18 $NaHCO_3$ mM, 2.4 $CaCl_2$ mM) at 32°C and for sIPSC recordings the solution was supplemented with 2mM of kynurenic acid. The aCSF solution was perfused over slices at ~2 mL/min.

To determine excitability, cells were patched with electrodes were filled with an internal solution (in mM: 130 potassium gluconate, 10 HEPES, 5 NaCl, 1 EGTA, 5 Mg-ATP, 0.5 Na-GTP, pH 7.3, 280 mOsm). Current-voltage curves were generated by recording in current-clamp mode and injecting steps of current (0–80-pA, 10-pA steps, 1-s) (both at resting membrane potential and at −60 mV). For sIPSCs, cells were patched with electrodes were filled with an internal solution (in mM: 135 KCl, 12 NaCl, 0.5 EGTA, 10 HEPES, 2.5 Mg-ATP, 0.25 sodium GTP, pH 7.3, 280 mOsm) and held at −60 mV. Recordings were analyzed using Clampfit (Molecular Devices). Excitability was calculated as the total number of events during each current step detected using the Event Detection function in Clampfit (50-ms before and 150-ms after action potential peak). The first action potential evoked from a 20-pA current injection while holding at −60mV were detected using the Event Detection threshold function in Clampfit. Hyperpolarization-induced rebound activity was assessed by injecting a hyperpolarizing step of current (−120-pA, 1-s). sIPSCS were detected using the Event Detection template function in Clampfit to determine frequency and amplitude.

**Retrograde tracing—**Mice were perfused and brains were collected for imaging (see immunohistochemistry and image analysis) nine days following rabies virus injection (see surgery). Then we optically cleared whole-brain samples using the SmartClear full active pipeline protocol (LifeCanvas Technologies, v5.05) for aqueous-based brain clearing and mounting as described recently (Szelenyi et al., 2023). Native fluorescent signals from aqueous-based cleared brains were imaged horizontally using the SmartSPIM LSFM (LifeCanvas Technologies) at 4 μm near-isotropic pixel resolution in 2 channels: 488-nm for registration signal and helper virus-infected cells, and 563-nm for rabies virus-infected

Author Manuscript Author Manuscript Author Manuscript Author Manuscript

inputs cells. Laser power and acquisition settings were held constant for all genetic groups and their individuals. Cleared whole-brain samples were then placed in phosphate-buffered saline (PBS) for at least two 24 h washes at room temperature. Whole-brain samples were then mounted in 4% agarose and sectioned into 50 μm sections using a vibratome for posthoc immunostaining of free-floating sections (see immunohistochemistry and image analysis).

**Immunohistochemistry and image analysis—**Mice were deeply anesthetized using Beuthanasia and transcardially perfused with phosphate-buffered saline (PBS), followed by 4% paraformaldehyde (PFA) in PBS. Brains were placed in 4% PFA overnight, then transferred to 30% sucrose in PBS solution at 4 ° C for at least 24 h. Brains were then sectioned into 30–40 μm sections using a cryostat and placed in PBS at 4 ° C. Brain sections were then stained to validate virus expression. Free-floating sections were placed in blocking buffer (3% normal donkey serum and 0.3% Triton X-100 in PBS) for 30-min. For enhancement of GCaMP6m, ChR2-YFP, JAWS-GFP, TC66T-2A-eGFP, and eYFP, sections were incubated in primary antibody (Chicken-GFP, 1:6000 dilution, ABCAM) overnight at 4 ° C. For enhancement of Chrimson-TdTomato, sections were incubated in primary antibody (Rabbit-DsRed, 1:1000 dilution, Takara) overnight at 4 ° C. For detection of tyrosine hydroxylase sections were incubated in primary antibody (Rabbit-Tyrosine Hydroxylase, 1:1000 dilution, Millipore Sigma) overnight at 4 ° C. Sections were then placed in PBS for three 10-min washes, and incubated in secondary antibody (Alexa Fluor 488 AffiniPure Donkey Anti-Chicken or Cy3 Donkey Anti-Rabbit, Jackson ImmunoResearch) for 1-h at room temperature. Then, following three 10-min PBS washes, sections were mounted using a mounting medium (DAPI Fluoromount-G, Southern Biotech) and cover-slipped. Images were taken using a KEYENCE BZ-X fluorescence microscope (KEYENCE). Histology sections from mice with optic fiber implants were used to identify optic fiber tip locations. One section containing the optic fiber tip location per mouse was used for the cell count and fluorescence intensity quantification of GCaMP-positive cells for the mice used in fiber photometry experiments during behavior. A custom CellProfiler 4.1.3 pipeline was used for quantification of GCaMP-positive cells in the photometry experiment and GFP-positive starter cells in the rabies tracing experiment. Fluorescence intensity was normalized to the maximum intensity per section. Representative histology images were registered to the Allen Brain Atlas using the ‘Wholebrain’ package[84] in R.

## QUANTIFICATION AND STATISTICAL ANALYSIS

**Statistical analysis—**All data are expressed as mean ± SEM. Statistical analyses were performed using GraphPad Prism, Python, and MATLAB. All statistical tests were two-tailed. Sample sizes were not predetermined using statistical methods. For data from two groups, the paired *t* test, unpaired *t* test, and Mann-Whitney *U* test were used where appropriate. For data from three or more groups, one-way ANOVA and one-way repeated-measures ANOVA followed by multiple-comparisons tests (Tukey’s multiple comparisons test, Bonferroni’s multiple comparisons test, two-stage linear step-up procedure of Bejamini, Krieger and Yekutieli) were used to determine any statistically significant differences between groups. For data from three or more groups and across multiple conditions, two-way ANOVA and two-way repeated-measures ANOVA followed by multiple-comparisons

Author Manuscript Author Manuscript Author Manuscript Author Manuscript

tests (Šídák's multiple comparisons test, two-stage linear step-up procedure of Bejamini, Krieger and Yekutieli) were used where appropriate. For correlation analysis, the Pearson correlation coefficient was used. For all tests, a significance threshold of 0.05 was used. See Table S1 for detailed statistical results.

**Linear encoding model—**To quantify the relative contribution of task variables to neural activity, we used a linear encoding model.[7,61] Multiple linear regression was used to predict the photometry signal for a given mouse using task behavioral variables as predictors. The task predictor set consisted of a matrix of 10 behavior event types (event times of trial initiation lever press, non-trial active lever press, non-trial inactive lever press, cue onset, reward outcome, omission outcome, rewarded port entry, unrewarded port entry, non-trial port entry, trial-reset house light cue). Each event type time series was convolved with a set of cubic splines that span several seconds after the event and 3 s before an action event type. A longer set of cubic splines was used for rewarded and unrewarded trial outcome events to reflect the longer trial outcome neural responses. The encoding model is expressed as $y = \beta X + \varepsilon$ where y is the GCaMP6m fluorescence for a given mouse during the random reward-omission task, X is the set of event predictors generated from the convolution of event times with the cubic spline set, and β is the set of weights learned from the regression.

We first fit the full version of the encoding model using the 'fitglm' function in MATLAB with 3-fold cross-validation to generate $R^2$ for the full model. We then compared the model fit when each of the task predictors were removed to that of the full model to quantify the relative contribution of individual behavioral variables. An individual task predictor contribution was defined as the reduction in explained variance $\Delta R^2$ when that task predictor was removed from the model ($1 - R^2_{\text{partial}}/R^2_{\text{full}}$). The relative contribution of an individual task predictor was defined as a fraction of the predictor contribution over the full model predictor contributions.

**Reward outcome history RPE analysis—**We used linear regression to predict neural activity following trial outcome using trial outcome information from the current and five previous trials.[60] The z-scored GCaMP6m signal during a 2-s time bin prior to trial initiation was subtracted from the z-scored GCaMP6m signal from 0 to 20-s following trial outcome for each trial during the random reward-omission task. Current and previous trial outcomes were labeled 0 for omission and 1 for reward. Multiple linear regression was used to generate weights corresponding to the contribution of each of the current and five previous trial outcomes to the neural activity following the current trial outcome. The model is expressed as $y(t) = \beta_0 + \beta_1 T_{out}(t) + \beta_2 T_{out}(t-1) + \ldots + \beta_6 T_{out}(t-5)$, where y(t) is the mean z-scored GCaMP6m signal from 0 to 20-s on trial t, $T_{out}(t)$ is the trial outcome, and $\beta_i$ is the regression coefficient for trial $T_{out}(t-n)$. The regression coefficients for each trial lag were generated with the 'OLS' function from the 'linear_model' module in the Python 'statsmodels' package.

**Whole-brain image processing and quantification—**We used ImageJ software to crop whole-brain image stacks, transform from the horizontal to coronal plane, and export images as TIFF files for whole-brain analysis. Brains were registered to the Unified brain

Author Manuscript Author Manuscript Author Manuscript Author Manuscript

atlas and segmented dsRed cell counts were partitioned into regions with Unified atlas labels.[87] For brain atlas registration and automated cell detection a previously described and modified ClearMap analysis pipeline[68,69] was used with minor adjustments. Accordingly, cell segmentation was automated using the Spot Detection function. The number of DsRed-positive input neurons per brain region was normalized to the total volume of the brain region from the reference atlas to calculate cell density per region (cells/$mm^3$). 3D renders of input cell location in atlas space were generated using the 'Wholebrain'[84] and 'SMART'[85] packages in R.

## Supplementary Material

Refer to Web version on PubMed Central for supplementary material.

## ACKNOWLEDGMENTS

This work was supported by NIH grants R01DA044315, R01MH104450 (L.S.Z.), F31DA053724 (J.E.E.), K99DA054265, R00DA054265 (B.J.), R00DA045662, and R01DA059374 (S.A.G.) and core grant P30DA048736 (University of Washington Center of Excellence in Opioid Addiction Research). We thank Dr. James Allen and Dr. Selena Schattauer for assistance in AAV production and members of the Zweifel laboratory for thoughtful discussion and transgenic mouse colony management. We thank Richard Palmiter, Garret Stuber, and Michael Bruchas for feedback.

## REFERENCES

1. Schultz W, Dayan P, and Montague PR (1997). A neural substrate of prediction and reward. Science 275, 1593–1599. [PubMed: 9054347]
2. O'Doherty JP, Cockburn J, and Pauli WM (2017). Learning, Reward, and Decision Making. Annu. Rev. Psychol. 68, 73–100. [PubMed: 27687119]
3. Berridge KC, and Robinson TE (1998). What is the role of dopamine in reward: hedonic impact, reward learning, or incentive salience? Brain Res. Brain Res. Rev. 28, 309–369. [PubMed: 9858756]
4. Bromberg-Martin ES, Matsumoto M, and Hikosaka O (2010). Dopamine in motivational control: rewarding, aversive, and alerting. Neuron 68, 815–834. [PubMed: 21144997]
5. Niv Y, Daw ND, Joel D, and Dayan P (2007). Tonic dopamine: opportunity costs and the control of response vigor. Psychopharmacology (Berl) 191, 507–520. [PubMed: 17031711]
6. Salamone JD, Wisniecki A, Carlson BB, and Correa M (2001). Nucleus accumbens dopamine depletions make animals highly sensitive to high fixed ratio requirements but do not impair primary food reinforcement. Neuroscience 105, 863–870. [PubMed: 11530224]
7. Engelhard B, Finkelstein J, Cox J, Fleming W, Jang HJ, Ornelas S, Koay SA, Thiberge SY, Daw ND, Tank DW, and Witten IB (2019). Specialized coding of sensory, motor and cognitive variables in VTA dopamine neurons. Nature 570, 509–513. [PubMed: 31142844]
8. Markowitz JE, Gillis WF, Jay M, Wood J, Harris RW, Cieszkowski R, Scott R, Brann D, Koveal D, Kula T, et al. (2023). Spontaneous behaviour is structured by reinforcement without explicit reward. Nature 614, 108–117. [PubMed: 36653449]
9. Harris JJ, Kollo M, Erskine A, Schaefer A, and Burdakov D (2022). Natural VTA activity during NREM sleep influences future exploratory behavior. iScience 25, 104396. [PubMed: 35663010]
10. Saddoris MP, Cacciapaglia F, Wightman RM, and Carelli RM (2015). Differential Dopamine Release Dynamics in the Nucleus Accumbens Core and Shell Reveal Complementary Signals for Error Prediction and Incentive Motivation. J. Neurosci. 35, 11572–11582. [PubMed: 26290234]
11. Cox J, and Witten IB (2019). Striatal circuits for reward learning and decision-making. Nat. Rev. Neurosci. 20, 482–494. [PubMed: 31171839]
12. Adcock RA, Thangavel A, Whitfield-Gabrieli S, Knutson B, and Gabrieli JDE (2006). Reward-motivated learning: mesolimbic activation precedes memory formation. Neuron 50, 507–517. [PubMed: 16675403]

Author Manuscript Author Manuscript Author Manuscript Author Manuscript

13. Choi JY, Jang HJ, Ornelas S, Fleming WT, Fürth D, Au J, Bandi A, Engel EA, and Witten IB (2020). A Comparison of Dopaminergic and Cholinergic Populations Reveals Unique Contributions of VTA Dopamine Neurons to Short-Term Memory. Cell Rep. 33, 108492. [PubMed: 33326775]
14. Eban-Rothschild A, Rothschild G, Giardino WJ, Jones JR, and de Lecea L (2016). VTA dopaminergic neurons regulate ethologically relevant sleep-wake behaviors. Nat. Neurosci. 19, 1356–1366. [PubMed: 27595385]
15. Gunaydin LA, Grosenick L, Finkelstein JC, Kauvar IV, Fenno LE, Adhikari A, Lammel S, Mirzabekov JJ, Airan RD, Zalocusky KA, et al. (2014). Natural neural projection dynamics underlying social behavior. Cell 157, 1535–1551. [PubMed: 24949967]
16. Solie C, Girard B, Righetti B, Tapparel M, and Bellone C (2022). VTA dopamine neuron activity encodes social interaction and promotes reinforcement learning through social prediction error. Nat. Neurosci. 25, 86–97. [PubMed: 34857949]
17. Torquet N, Marti F, Campart C, Tolu S, Nguyen C, Oberto V, Benallaoua M, Naudé J, Didienne S, Debray N, et al. (2018). Social interactions impact on the dopaminergic system and drive individuality. Nat. Commun. 9, 3081. [PubMed: 30082725]
18. Bakhurin KI, Hughes RN, Jiang Q, Hossain M, Gutkin B, Fallon IP, and Yee HH (2023). Force tuning explains changes in phasic dopamine signaling during stimulus-reward learning. Preprint at bioRxiv, 537994. 10.1101/2023.04.23.537994.2023.04.23.
19. Grove JCR, Gray LA, La Santa Medina N, Sivakumar N, Ahn JS, Corpuz TV, Berke JD, Kreitzer AC, and Knight ZA (2022). Dopamine subsystems that track internal states. Nature 608, 374–380. [PubMed: 35831501]
20. Brischoux F, Chakraborty S, Brierley DI, and Ungless MA (2009). Phasic excitation of dopamine neurons in ventral VTA by noxious stimuli. Proc. Natl. Acad. Sci. USA 106, 4894–4899. [PubMed: 19261850]
21. Horvitz JC (2000). Mesolimbocortical and nigrostriatal dopamine responses to salient non-reward events. Neuroscience 96, 651–656. [PubMed: 10727783]
22. Lammel S, Ion DI, Roeper J, and Malenka RC (2011). Projection-specific modulation of dopamine neuron synapses by aversive and rewarding stimuli. Neuron 70, 855–862. [PubMed: 21658580]
23. Zweifel LS, Fadok JP, Argilli E, Garelick MG, Jones GL, Dickerson TMK, Allen JM, Mizumori SJY, Bonci A, and Palmiter RD (2011). Activation of dopamine neurons is critical for aversive conditioning and prevention of generalized anxiety. Nat. Neurosci. 14, 620–626. [PubMed: 21499253]
24. Jo YS, Heymann G, and Zweifel LS (2018). Dopamine Neurons Reflect the Uncertainty in Fear Generalization. Neuron 100, 916–925.e3. [PubMed: 30318411]
25. Cai LX, Pizano K, Gundersen GW, Hayes CL, Fleming WT, Holt S, Cox JM, and Witten IB (2020). Distinct signals in medial and lateral VTA dopamine neurons modulate fear extinction at different times. Elife 9, e54936. [PubMed: 32519951]
26. Salinas-Hernandez XI, Vogel P, Betz S, Kalisch R, Sigurdsson T, and Duvarci S (2018). Dopamine neurons drive fear extinction learning by signaling the omission of expected aversive outcomes. Elife 7, e38818. [PubMed: 30421719]
27. Lammel S, Lim BK, Ran C, Huang KW, Betley MJ, Tye KM, Deisseroth K, and Malenka RC (2012). Input-specific control of reward and aversion in the ventral tegmental area. Nature 491, 212–217. [PubMed: 23064228]
28. Morales M, and Margolis EB (2017). Ventral tegmental area: cellular heterogeneity, connectivity and behaviour. Nat. Rev. Neurosci. 18, 73–85. [PubMed: 28053327]
29. Poulin JF, Caronia G, Hofer C, Cui Q, Helm B, Ramakrishnan C, Chan CS, Dombeck DA, Deisseroth K, and Awatramani R (2018). Mapping projections of molecularly defined dopamine neuron subtypes using intersectional genetic approaches. Nat. Neurosci. 21, 1260–1271. [PubMed: 30104732]
30. Heymann G, Jo YS, Reichard KL, McFarland N, Chavkin C, Palmiter RD, Soden ME, and Zweifel LS (2020). Synergy of Distinct Dopamine Projection Populations in Behavioral Reinforcement. Neuron 105, 909–920.e5. [PubMed: 31879163]

Author Manuscript Author Manuscript Author Manuscript Author Manuscript


31. Mohebi A, Pettibone JR, Hamid AA, Wong JMT, Vinson LT, Patriarchi T, Tian L, Kennedy RT, and Berke JD (2019). Dissociable dopamine dynamics for learning and motivation. Nature 570, 65–70. [PubMed: 31118513]
32. Balleine BW, Delgado MR, and Hikosaka O (2007). The role of the dorsal striatum in reward and decision-making. J. Neurosci. 27, 8161–8165. [PubMed: 17670959]
33. O'Doherty J, Dayan P, Schultz J, Deichmann R, Friston K, and Dolan RJ (2004). Dissociable roles of ventral and dorsal striatum in instrumental conditioning. Science 304, 452–454. [PubMed: 15087550]
34. van Elzelingen W, Goedhoop J, Warnaar P, Denys D, Arbab T, and Willuhn I (2022). A unidirectional but not uniform striatal landscape of dopamine signaling for motivational stimuli. Proc. Natl. Acad. Sci. USA 119, e2117270119. [PubMed: 35594399]
35. de Jong JW, Liang Y, Verharen JPH, Fraser KM, and Lammel S (2024). State and rate-of-change encoding in parallel mesoaccumbal dopamine pathways. Nat. Neurosci. 27, 309–318. [PubMed: 38212586]
36. Saunders BT, Richard JM, Margolis EB, and Janak PH (2018). Dopamine neurons create Pavlovian conditioned stimuli with circuit-defined motivational properties. Nat. Neurosci. 21, 1072–1083. [PubMed: 30038277]
37. de Jong JW, Afjei SA, Pollak Dorocic I, Peck JR, Liu C, Kim CK, Tian L, Deisseroth K, and Lammel S (2019). A Neural Circuit Mechanism for Encoding Aversive Stimuli in the Mesolimbic Dopamine System. Neuron 101, 133–151.e7. [PubMed: 30503173]
38. Collins AL, and Saunders BT (2020). Heterogeneity in striatal dopamine circuits: Form and function in dynamic reward seeking. J. Neurosci. Res. 98, 1046–1069. [PubMed: 32056298]
39. Nair-Roberts RG, Chatelain-Badie SD, Benson E, White-Cooper H, Bolam JP, and Ungless MA (2008). Stereological estimates of dopaminergic, GABAergic and glutamatergic neurons in the ventral tegmental area, substantia nigra and retrorubral field in the rat. Neuroscience 152, 1024–1031. [PubMed: 18355970]
40. Phillips RA 3rd, Tuscher JJ, Black SL, Andraka E, Fitzgerald ND, Ianov L, and Day JJ (2022). An atlas of transcriptionally defined cell populations in the rat ventral tegmental area. Cell Rep. 39, 110616. [PubMed: 35385745]
41. Simon RC, Loveless MC, Yee JX, Goh B, Cho SG, Nasir Z, Hashikawa K, Stuber GD, Zweifel LS, and Soden ME (2024). Opto-seq reveals input-specific immediate-early gene induction in ventral tegmental area cell types. Neuron. S0896–6273:00373–00378.
42. Jhou TC, Fields HL, Baxter MG, Saper CB, and Holland PC (2009). The rostromedial tegmental nucleus (RMTg), a GABAergic afferent to midbrain dopamine neurons, encodes aversive stimuli and inhibits motor responses. Neuron 61, 786–800. [PubMed: 19285474]
43. Johnson SW, and North RA (1992). Two types of neurone in the rat ventral tegmental area and their synaptic inputs. J. Physiol. 450, 455–468. [PubMed: 1331427]
44. Soden ME, Chung AS, Cuevas B, Resnick JM, Awatramani R, and Zweifel LS (2020). Anatomic resolution of neurotransmitter-specific projections to the VTA reveals diversity of GABAergic inputs. Nat. Neurosci. 23, 968–980. [PubMed: 32541962]
45. Tan KR, Yvon C, Turiault M, Mirzabekov JJ, Doehner J, Labouèbe G, Deisseroth K, Tye KM, and Lüscher C (2012). GABA neurons of the VTA drive conditioned place aversion. Neuron 73, 1173–1183. [PubMed: 22445344]
46. van Zessen R, Phillips JL, Budygin EA, and Stuber GD (2012). Activation of VTA GABA neurons disrupts reward consumption. Neuron 73, 1184–1194. [PubMed: 22445345]
47. Eshel N, Bukwich M, Rao V, Hemmelder V, Tian J, and Uchida N (2015). Arithmetic and local circuitry underlying dopamine prediction errors. Nature 525, 243–246. [PubMed: 26322583]
48. Beier KT, Steinberg EE, DeLoach KE, Xie S, Miyamichi K, Schwarz L, Gao XJ, Kremer EJ, Malenka RC, and Luo L (2015). Circuit Architecture of VTA Dopamine Neurons Revealed by Systematic Input-Output Mapping. Cell 162, 622–634. [PubMed: 26232228]
49. Chung AS, Miller SM, Sun Y, Xu X, and Zweifel LS (2017). Sexual congruency in the connectome and translatome of VTA dopamine neurons. Sci. Rep. 7, 11120. [PubMed: 28894175]

Author Manuscript Author Manuscript Author Manuscript Author Manuscript


50. Faget L, Osakada F, Duan J, Ressler R, Johnson AB, Proudfoot JA, Yoo JH, Callaway EM, and Hnasko TS (2016). Afferent Inputs to Neurotransmitter-Defined Cell Types in the Ventral Tegmental Area. Cell Rep. 15, 2796–2808. [PubMed: 27292633]
51. Tian J, Huang R, Cohen JY, Osakada F,, Kobak D, Machens CK, Callaway EM, Uchida N, and Watabe-Uchida M (2016). Distributed and Mixed Information in Monosynaptic Inputs to Dopamine Neurons. Neuron 91, 1374–1389. [PubMed: 27618675]
52. Nieh EH, Vander Weele CM, Matthews GA, Presbrey KN, Wichmann R, Leppla CA, Izadmehr EM, and Tye KM (2016). Inhibitory Input from the Lateral Hypothalamus to the Ventral Tegmental Area Disinhibits Dopamine Neurons and Promotes Behavioral Activation. Neuron 90, 1286–1298. [PubMed: 27238864]
53. Yang H, de Jong JW, Tak Y, Peck J, Bateup HS, and Lammel S (2018). Nucleus Accumbens Subnuclei Regulate Motivated Behavior via Direct Inhibition and Disinhibition of VTA Dopamine Subpopulations. Neuron 97, 434–449.e4. [PubMed: 29307710]
54. Nugent AL, Anderson EM, Larson EB, and Self DW (2017). Incubation of cue-induced reinstatement of cocaine, but not sucrose, seeking in C57BL/6J mice. Pharmacol. Biochem. Behav. 159, 12–17. [PubMed: 28669705]
55. Soden ME, Yee JX, Cuevas B, Rastani A, Elum J, and Zweifel LS (2022). Distinct Encoding of Reward and Aversion by Peptidergic BNST Inputs to the VTA. Front. Neural Circ. 16, 918839.
56. Adamantidis AR, Tsai HC, Boutrel B, Zhang F, Stuber GD, Budygin EA, Touriño C, Bonci A, Deisseroth K, and de Lecea L (2011). Optogenetic interrogation of dopaminergic modulation of the multiple phases of reward-seeking behavior. J. Neurosci. 31, 10829–10835. [PubMed: 21795535]
57. Tsai HC, Zhang F, Adamantidis A, Stuber GD, Bonci A, de Lecea L, and Deisseroth K (2009). Phasic firing in dopaminergic neurons is sufficient for behavioral conditioning. Science 324, 1080–1084. [PubMed: 19389999]
58. Witten IB, Steinberg EE, Lee SY, Davidson TJ, Zalocusky KA, Brodsky M, Yizhar O, Cho SL, Gong S, Ramakrishnan C, et al. (2011). Recombinase-driver rat lines: tools, techniques, and optogenetic application to dopamine-mediated reinforcement. Neuron 72, 721–733. [PubMed: 22153370]
59. Eshel N, Tian J, Bukwich M, and Uchida N (2016). Dopamine neurons share common response function for reward prediction error. Nat. Neurosci. 19, 479–486. [PubMed: 26854803]
60. Bayer HM, and Glimcher PW (2005). Midbrain dopamine neurons encode a quantitative reward prediction error signal. Neuron 47, 129–141. [PubMed: 15996553]
61. Parker NF, Baidya A, Cox J, Haetzel LM, Zhukovskaya A, Murugan M, Engelhard B, Goldman MS, and Witten IB (2022). Choice-selective sequences dominate in cortical relative to thalamic inputs to NAc to support reinforcement learning. Cell Rep. 39, 110756. [PubMed: 35584665]
62. Gan JO, Walton ME, and Phillips PEM (2010). Dissociable cost and benefit encoding of future rewards by mesolimbic dopamine. Nat. Neurosci. 13, 25–27. [PubMed: 19904261]
63. Salamone JD, and Correa M (2012). The mysterious motivational functions of mesolimbic dopamine. Neuron 76, 470–485. [PubMed: 23141060]
64. Hodos W (1961). Progressive ratio as a measure of reward strength. Science 134, 943–944. [PubMed: 13714876]
65. Ogawa SK, Cohen JY, Hwang D, Uchida N, and Watabe-Uchida M (2014). Organization of monosynaptic inputs to the serotonin and dopamine neuromodulatory systems. Cell Rep. 8, 1105–1118. [PubMed: 25108805]
66. Watabe-Uchida M, Zhu L, Ogawa SK, Vamanrao A, and Uchida N (2012). Whole-brain mapping of direct inputs to midbrain dopamine neurons. Neuron 74, 858–873. [PubMed: 22681690]
67. Sun Y, Nguyen AQ, Nguyen JP, Le L, Saur D, Choi J, Callaway EM, and Xu X (2014). Cell-type-specific circuit connectivity of hippocampal CA1 revealed through Cre-dependent rabies tracing. Cell Rep. 7, 269–280. [PubMed: 24656815]
68. Madangopal R, Szelenyi ER, Nguyen J, Brenner MB, Drake OR, Pham DQ, Shekara A, Jin M, Choong JJ, Heins C, et al. (2022). Incubation of palatable food craving is associated with brain-wide neuronal activation in mice. Proc. Natl. Acad. Sci. USA 119, e2209382119. [PubMed: 36603188]

Author Manuscript Author Manuscript Author Manuscript Author Manuscript


69. Renier N, Adams EL, Kirst C, Wu Z, Azevedo R, Kohl J, Autry AE, Kadiri L, Umadevi Venkataraju K, Zhou Y, et al. (2016). Mapping of Brain Activity by Automated Volume Analysis of Immediate Early Genes. Cell 165, 1789–1802. [PubMed: 27238021]
70. Xu N, LaGrow TJ, Anumba N, Lee A, Zhang X, Yousefi B, Bassil Y, Clavijo GP, Khalilzad Sharghi V, Maltbie E, et al. (2022). Functional Connectivity of the Brain Across Rodents and Humans. Front. Neurosci. 16, 816331. [PubMed: 35350561]
71. Schultz W (1998). Predictive reward signal of dopamine neurons. J. Neurophysiol. 80, 1–27. [PubMed: 9658025]
72. Farrell K, Lak A, and Saleem AB (2022). Midbrain dopamine neurons signal phasic and ramping reward prediction error during goal-directed navigation. Cell Rep. 41, 111470. [PubMed: 36223748]
73. Hamid AA, Pettibone JR, Mabrouk OS, Hetrick VL, Schmidt R, Vander Weele CM, Kennedy RT, Aragona BJ, and Berke JD (2016). Mesolimbic dopamine signals the value of work. Nat. Neurosci. 19, 117–126. [PubMed: 26595651]
74. Howe MW, Tierney PL, Sandberg SG, Phillips PEM, and Graybiel AM (2013). Prolonged dopamine signalling in striatum signals proximity and value of distant rewards. Nature 500, 575–579. [PubMed: 23913271]
75. Wassum KM, Ostlund SB, and Maidment NT (2012). Phasic mesolimbic dopamine signaling precedes and predicts performance of a self-initiated action sequence task. Biol. Psychiatr. 71, 846–854.
76. Glasgow SD, McPhedrain R, Madranges JF, Kennedy TE, and Ruthazer ES (2019). Approaches and Limitations in the Investigation of Synaptic Transmission and Plasticity. Front. Synaptic Neurosci. 11, 20. [PubMed: 31396073]
77. Segal M (2010). Dendritic spines, synaptic plasticity and neuronal survival: activity shapes dendritic spines to enhance neuronal viability. Eur. J. Neurosci. 31, 2178–2184. [PubMed: 20550565]
78. Dixon C, Sah P, Lynch JW, and Keramidas A (2014). GABAA receptor alpha and gamma subunits shape synaptic currents via different mechanisms. J. Biol. Chem. 289, 5399–5411. [PubMed: 24425869]
79. Farrant M, and Kaila K (2007). The cellular, molecular and ionic basis of GABA(A) receptor signalling. Prog. Brain Res. 160, 59–87. [PubMed: 17499109]
80. Soden ME, Yee JX, and Zweifel LS (2023). Circuit coordination of opposing neuropeptide and neurotransmitter signals. Nature 619, 332–337. [PubMed: 37380765]
81. Simpson EH, Akam T, Patriarchi T, Blanco-Pozo M, Burgeno LM, Mohebi A, Cragg SJ, and Walton ME (2024). Lights, fiber, action! A primer on in vivo fiber photometry. Neuron 112, 718–739. [PubMed: 38103545]
82. Schindelin J, Arganda-Carreras I, Frise E, Kaynig V, Longair M, Pietzsch T, Preibisch S, Rueden C, Saalfeld S, Schmid B, et al. (2012). Fiji: an open-source platform for biological-image analysis. Nat. Methods. 9, 676. [PubMed: 22743772]
83. McQuin C, Goodman A, Chernyshev V, Kamentsky L, Cimini BA, Karhohs KW, Doan M, Ding L, Rafeslski SM, Thirstrup D, et al. (2018). CellProfiler 3.0: Next-generation image processing for biology. Plos Biol. 3, 16.
84. Furth D, Vaissiere T, Tzortzi O, Xuan Y, Martin A, Lazardis I, Spigolon G, Fisone G, Tomer R, Deisseroth K, et al. (2018). An interactive framework for whole-brain maps at cellular resolution. Nat. Neurosci. 21, 139–149. [PubMed: 29203898]
85. Jin M, Nguyen JD, Weber SJ, Mejias-Aponte CA, Madangopal R, and Golden SA (2022). SMART: An Open-Source Extension of WholeBrain for Intact Mouse Brain Registration and Segmentation. eNeuro 9, ENEURO.0482–21.2022.
86. Sanford CA, Soden ME, Baird MA, Miller SM, Schulkin J, Palmiter RD, Clark M, and Zweifel LS (2017). A Central Amygdala CRF Circuit Facilitates Learning about Weak Threats. Neuron 93, 164–178. [PubMed: 28017470]
87. Chon U, Vanselow DJ, Cheng KC, and Kim Y (2019). Enhanced and unified anatomical labeling for a common mouse brain atlas. Nat. Commun. 10, 5067. [PubMed: 31699990]

Author Manuscript Author Manuscript Author Manuscript Author Manuscript

## Highlights

- Differential encoding of task-specific variables by dopamine subpopulations and GABA neurons
- Differential encoding of motivated responses by dopamine subpopulations and GABA neurons
- Dopamine subpopulations have different intrinsic properties and connectivity

Author Manuscript Author Manuscript Author Manuscript Author Manuscript

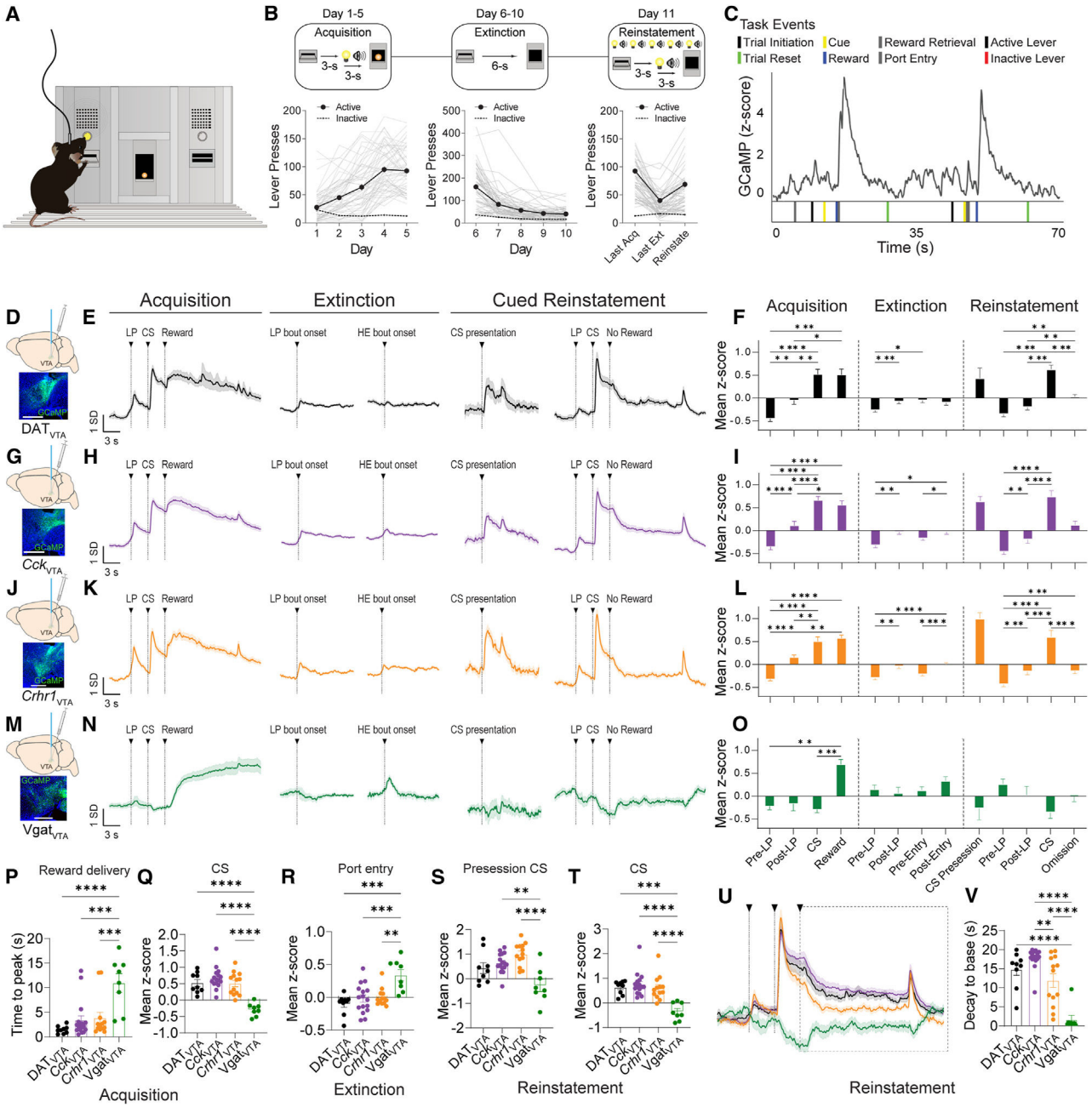


**Figure 1. Fiber photometry during cued reinstatement**

(A) Schematic of a fiber photometry session.

(B) Schematic depicting training and performance of mice ($n$ = 57 mice; solid lines indicate mean across mice, and gray lines indicate individual replicates).

(C) Example recording trace during acquisition showing GCaMP fluorescence (top) aligned to event timestamps (bottom).

(D) Schematic of viral injection and optic fiber implant and example histology image from the VTA showing GCaMP6 (green) in the $DAT_{VTA}$ group. Scale bar: 500 μm.

(E) Z scored GCaMP fluorescence from $DAT_{VTA}$ population recordings aligned to task events ($n$ = 9 mice, 63 sessions). Data are from all trials during the first, third, and last

Author Manuscript Author Manuscript Author Manuscript Author Manuscript

acquisition and extinction training sessions and from all trials during the reinstatement session.

(F) Average Z scored GCaMP fluorescence from $DAT_{VTA}$ population recordings during LP, CS, reward, port entry, and omission periods ($n$ = 9 mice, 63 sessions, bars and error bars indicate mean ± SEM across mice; see Table S1 for statistical values).

(G) Same as in (D) but for $Cck_{VTA}$ population recordings. Scale bar: 500 μm.

(H) Same as in (E) but for $Cck_{VTA}$ population recordings ($n$ = 16 mice, 112 sessions).

(I) Same as in (F) but for $Cck_{VTA}$ population recordings ($n$ = 16 mice, 112 sessions).

(J) Same as in (D) but for $Crhr1_{VTA}$ population recordings. Scale bar: 500 μm.

(K) Same as in (E) but for $Crhr1_{VTA}$ population recordings ($n$ = 13 mice, 91 sessions).

(L) Same as in (F) but for $Crhr1_{VTA}$ population recordings ($n$ = 13 mice, 91 sessions).

(M) Same as in (D) but for $Vgat_{VTA}$ population recordings. Scale bar: 500 μm.

(N) Same as in (E) but for $Vgat_{VTA}$ population recordings ($n$ = 8 mice, 56 sessions).

(O) Same as in (F) but for $Vgat_{VTA}$ population recordings ($n$ = 8 mice, 56 sessions).

(P) Average latency to peak of $Z$ scored GCaMP fluorescence following reward delivery during acquisition for $DAT_{VTA}$ ($n$ = 9 mice), $Cck_{VTA}$ ($n$ = 16 mice), $Crhr1_{VTA}$ ($n$ = 13 mice), and $Vgat_{VTA}$ ($n$ = 8 mice) groups.

(Q) Average $Z$ scored GCaMP fluorescence during CS presentation period following reward delivery during acquisition for $DAT_{VTA}$ ($n$ = 9 mice), $Cck_{VTA}$ ($n$ = 16 mice), $Crhr1_{VTA}$ ($n$ = 13 mice), and $Vgat_{VTA}$ ($n$ = 8 mice) groups.

(R) Average $Z$ scored GCaMP fluorescence during port entry period during extinction phase of cued reinstatement for $DAT_{VTA}$ ($n$ = 9 mice), $Cck_{VTA}$ ($n$ = 16 mice), $Crhr1_{VTA}$ ($n$ = 13 mice), and $Vgat_{VTA}$ ($n$ = 8 mice) groups.

(S) Average $Z$ scored GCaMP fluorescence during CS presentation periods during reinstatement presession for $DAT_{VTA}$ ($n$ = 9 mice), $Cck_{VTA}$ ($n$ = 16 mice), $Crhr1_{VTA}$ ($n$ = 13 mice), and $Vgat_{VTA}$ ($n$ = 8 mice) groups.

(T) Average $Z$ scored GCaMP fluorescence during CS presentation periods during reinstatement session for $DAT_{VTA}$ ($n$ = 9 mice), $Cck_{VTA}$ ($n$ = 16 mice), $Crhr1_{VTA}$ ($n$ = 13), and $Vgat_{VTA}$ ($n$ = 8 mice) groups.

(U) $Z$ scored GCaMP fluorescence aligned to reward omission period during reinstatement phase in $DAT_{VTA}$ ($n$ = 9 mice), $Cck_{VTA}$ ($n$ = 16 mice), $Crhr1_{VTA}$ ($n$ = 13 mice), and $Vgat_{VTA}$ ($n$ = 8 mice) groups. Dotted rectangle indicates mean Z score analysis epoch.

(V) Average latency to minimum GCaMP fluorescence during reward omission period during reinstatement for $DAT_{VTA}$ ($n$ = 9 mice), $Cck_{VTA}$ ($n$ = 16 mice), $Crhr1_{VTA}$ ($n$ = 13 mice), and $Vgat_{VTA}$ ($n$ = 8 mice) groups. Bars and error bars indicate mean ± SEM across mice (see Table S1 for statistical values).

Author Manuscript Author Manuscript Author Manuscript Author Manuscript

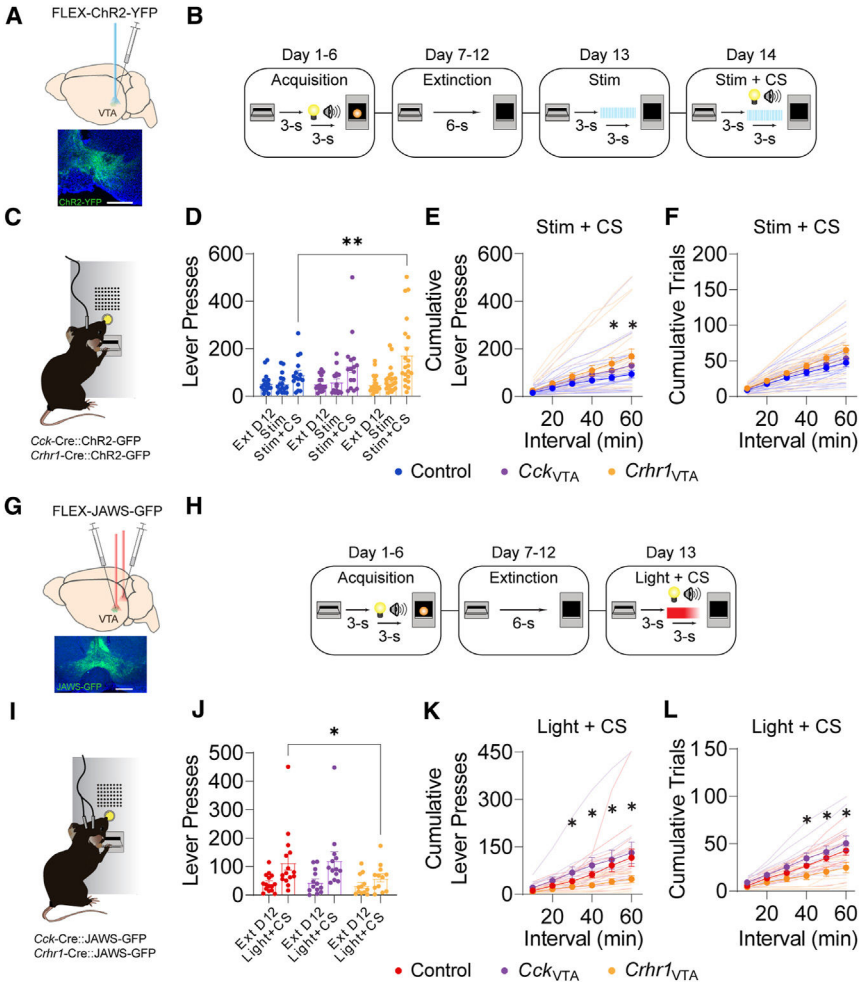


**Figure 2. Photostimulation and photoinhibition of *Crhr1*$_{VTA}$ and *Cck*$_{VTA}$ neurons during cued reinstatement**

(A) Schematic of viral injection and optic fiber implant and example histology image from the VTA showing staining for ChR2-YFP (green) in VTA subpopulations.

(B) Schematic of the training phases of the optogenetic cued reinstatement task.

(C) Schematic of an optogenetic cued reinstatement session.

(D) Mean number of lever presses across mice during acquisition and extinction sessions in control, *Cck*$_{VTA}$, and *Crhr1*$_{VTA}$ groups ($n$ = 11–21 mice, error bars represent SEM).

(E) Mean number of cumulative lever presses on day 14 (Stim + CS) with optogenetic activation or in control mice without opsin expression ($n$ = 11–21 mice, error bars indicate SEM).

(F) Mean number of cumulative trials completed on day 14 (Stim + CS) with optogenetic activation or in control mice without opsin expression ($n$ = 11–21 mice, error bars indicate SEM).

(G) Schematic of viral injection and optic fiber implant and example histology image from the VTA showing staining for JAWS-GFP (green) in VTA subpopulations.

(H) Schematic of the training phases of the opto-genetic cued reinstatement task.

(I) Schematic of an optogenetic cued reinstatement session.

Author Manuscript Author Manuscript Author Manuscript Author Manuscript

(J) Mean number of lever presses on day 12 (extinction [Ext] D12), and day 13 (Light + CS) with optogenetic inhibition or in control mice without opsin expression ($n$ = 12–14 mice, error bars indicate SEM).

(K) Mean number of cumulative lever presses on day 13 (Light + CS) with optogenetic inhibition or in control mice without opsin expression ($n$ = 12–14 mice, error bars indicate SEM).

(L) Mean number of cumulative trials completed on day 13 (Light + CS) with optogenetic inhibition or in control mice without opsin expression ($n$ = 12–14 mice, error bars indicate SEM; see Table S1 for statistical values).

Author Manuscript Author Manuscript Author Manuscript Author Manuscript

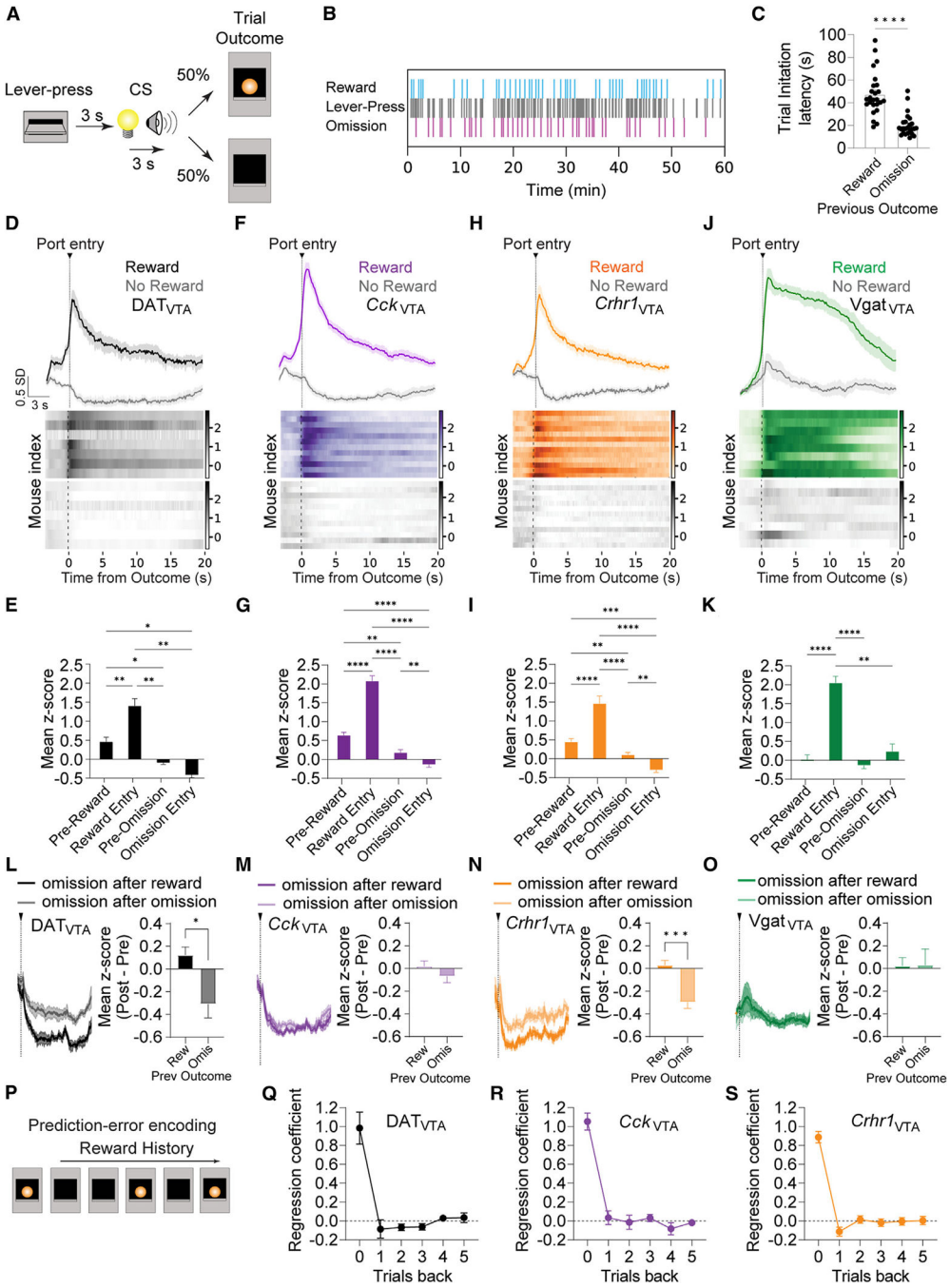


**Figure 3. Time-locked activation of VTA subpopulations during random reward omission**

(A) Schematic of the random reward omission task; probability of reward was 50%.

(B) Example behavioral session showing lever press, reward, and omission times.

(C) Trial initiation latency following the intertrial interval period ($n = 25$ mice, bars and error bars indicate mean ± SEM across mice).

(D) $Z$ scored GCaMP fluorescence and heatmaps aligned to reward (color) or reward omission (gray) task events from the $DAT_{VTA}$ group ($n = 7$ mice).

Author Manuscript Author Manuscript Author Manuscript Author Manuscript

(E) Average *Z* scored GCaMP fluorescence during reward, omission, and port entry periods for the $DAT_{VTA}$ (*n* = 7 mice) group.
(F) Same as in (D) but for the $Cck_{VTA}$ (*n* = 12 mice) group.
(G) Same as in (E) but for the $Cck_{VTA}$ (*n* = 12 mice) group.
(H) Same as in (D) but for the $Crhr1_{VTA}$ (*n* = 13 mice) group.
(I) Same as in (E) but for the $Crhr1_{VTA}$ (*n* = 13 mice) group.
(J) Same as in (D) but for the $Vgat_{VTA}$ (*n* = 8 mice) group.
(K) Same as in (E) but for the $Vgat_{VTA}$ (*n* = 8 mice) group.
(L) *Z* scored GCaMP fluorescence (left) and average *Z* scored GCaMP fluorescence (right) during reward omission periods shaded according to previous trial outcome type for the $DAT_{VTA}$ group (*n* = 7 mice).
(M) Same as in (L) but for the $Cck_{VTA}$ group (*n* = 12 mice).
(N) Same as in (L) but for the $Crhr1_{VTA}$ group (*n* = 13 mice).
(O) Same as in (L) but for the $Vgat_{VTA}$ group (*n* = 8 mice).
(P) Schematic of outcome history regression model approach. The current previous five trial outcomes were used with a multiple linear regression to predict the GCaMP signal during the current trial outcome.
(Q) Average regression coefficients across mice for the outcome history linear regression for $DAT_{VTA}$ (*n* = 7 mice), $Cck_{VTA}$ neurons (left) (*n* = 12 mice), and $Crhr1_{VTA}$ neurons (right) (*n* = 13 mice; see Table S1 for statistical values).
(R) Same as in (Q) but for the $Cck_{VTA}$ group (*n* = 12 mice).
(S) Same as in (Q) but for the $Crhr1_{VTA}$ group (*n* = 13 mice).

Author Manuscript Author Manuscript Author Manuscript Author Manuscript

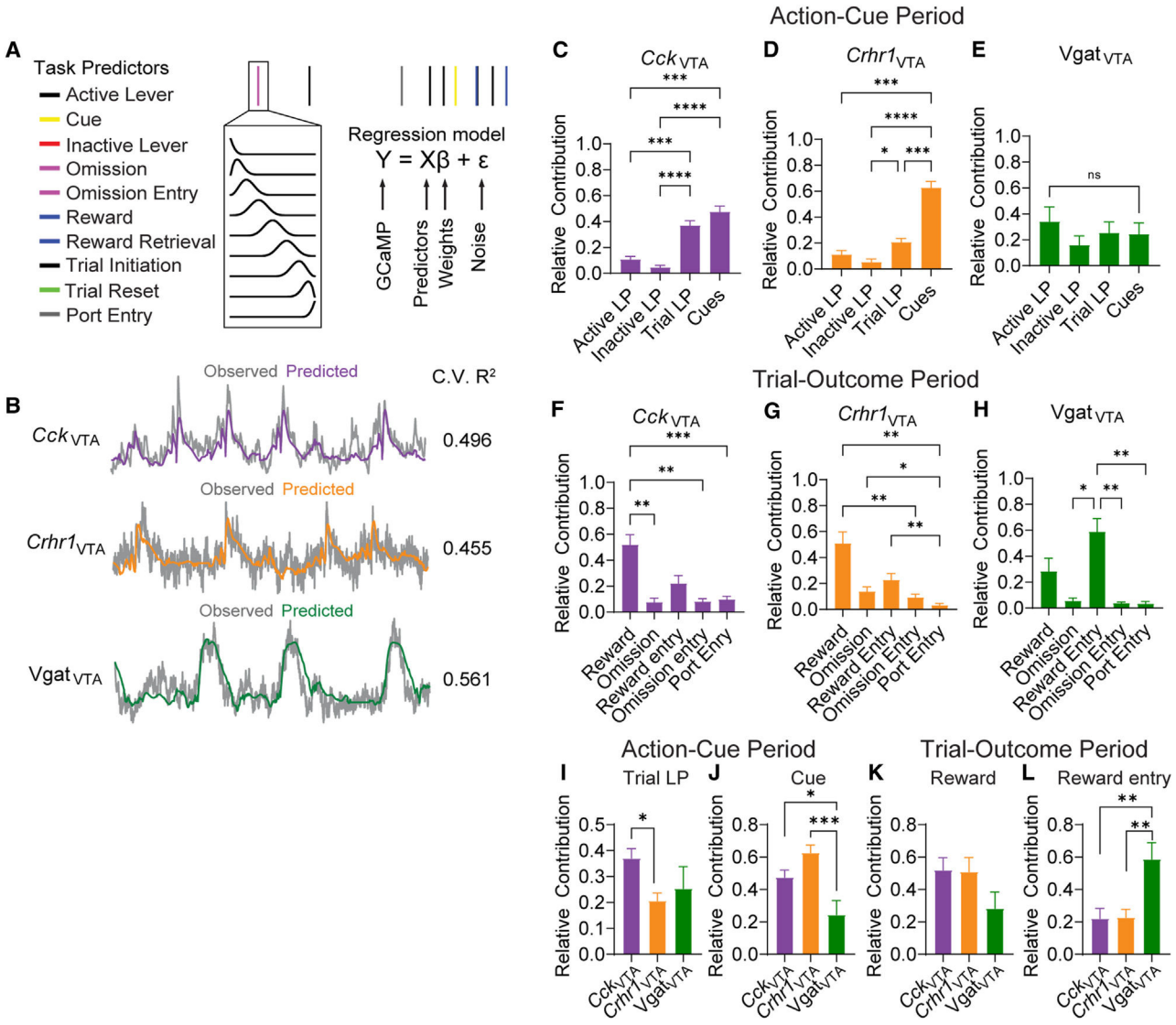


**Figure 4. Differential encoding of task-relevant behavioral variables during random reward omission**

(A) Schematic of the linear encoding model. Task event timestamps were convolved with a set of cubic splines to generate a predictor set of ten behavior event types. The GCaMP signal was predicted based on task events.

(B) Example observed (gray) and predicted (color) GCaMP traces from *Cck*$_{VTA}$ (top), *Crhr1*$_{VTA}$ (middle), and Vgat$_{VTA}$ (bottom) groups.

(C) Relative contribution of each task event type to the explained variance of the GCaMP signal during the action cue period averaged across mice for the *Cck*$_{VTA}$ group ($n$ = 12 mice) (see Table S1 for statistical values).

(D) Same as in (C) but for the *Crhr1*$_{VTA}$ group ($n$ = 11 mice).

(E) Same as in (C) but for the Vgat$_{VTA}$ group ($n$ = 8 mice).

(F) Relative contribution of each task event type to the explained variance of the GCaMP signal during the trial outcome period averaged across mice for the *Cck*$_{VTA}$ group ($n$ = 12 mice).

Author Manuscript Author Manuscript Author Manuscript Author Manuscript

(G) Same as in (F) but for the *Crhr1*$_{VTA}$ group ($n$ = 11 mice).
(H) Same as in (F) but for the Vgat$_{VTA}$ group ($n$ = 8 mice).
(I) Relative contribution of trial lever press during action cue period average across mice for *Cck*$_{VTA}$ ($n$ = 12 mice), *Crhr1*$_{VTA}$ ($n$ = 11 mice), and Vgat$_{VTA}$ ($n$ = 8 mice) groups (see Table S1 for statistical values).
(J) Relative contribution of the cue during action cue period average across mice for *Cck*$_{VTA}$ ($n$ = 12 mice), *Crhr1*$_{VTA}$ ($n$ = 11 mice), and Vgat$_{VTA}$ ($n$ = 8 mice) groups (see Table S1 for statistical values).
(K) Relative contribution of reward during trial outcome period average across mice for *Cck*$_{VTA}$ ($n$ = 12 mice), *Crhr1*$_{VTA}$ ($n$ = 11 mice), and Vgat$_{VTA}$ ($n$ = 8 mice) groups (see Table S1 for statistical values).
(L) Relative contribution of reward entry during trial outcome period average across mice for *Cck*$_{VTA}$ ($n$ = 12 mice), *Crhr1*$_{VTA}$ ($n$ = 11 mice), and Vgat$_{VTA}$ ($n$ = 8 mice) groups (see Table S1 for statistical values).

Author Manuscript Author Manuscript Author Manuscript Author Manuscript

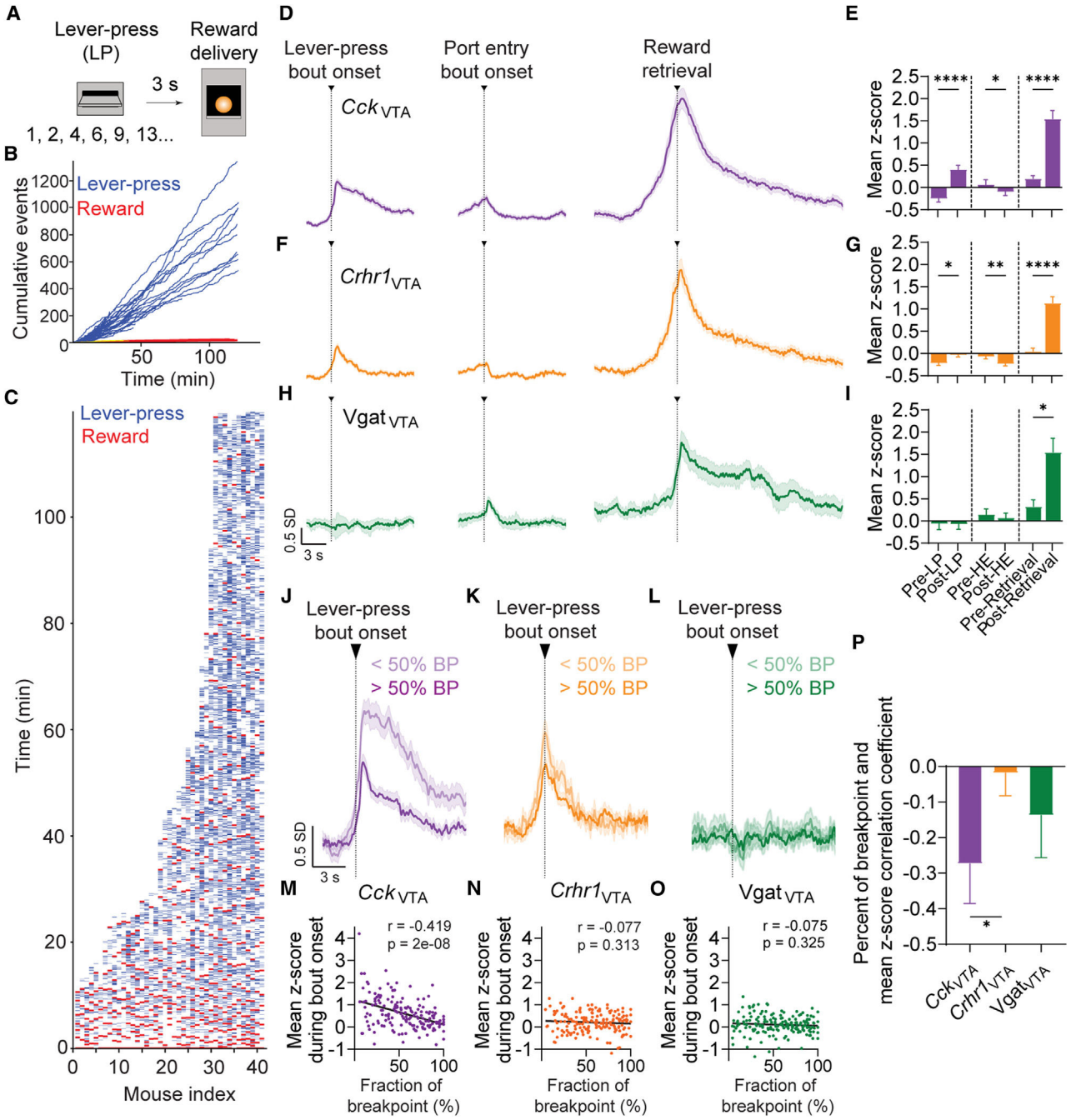


**Figure 5. Differential encoding of motivated responses**

Schematic of the progressive ratio (PR) task.

(A) Cumulative lever presses (blue) and rewards (red) during PR sessions. Lines indicate individual mice ($n = 42$ mice).

(B) Lever press (blue) and reward (red) event times shown for all sessions ($n = 42$ mice).

(C) $Z$ scored GCaMP fluorescence from photometry recordings aligned to lever press bout onset, port entry bout onset, and reward retrieval for $Cck_{VTA}$ group ($n = 17$ mice).

Author Manuscript Author Manuscript Author Manuscript Author Manuscript

(D) Average *Z* scored GCaMP fluorescence during lever press bout onset, port entry bout onset, and reward retrieval periods for the $Cck_{VTA}$ group ($n$ = 17 mice). Bars and error bars indicate mean ± SEM across mice.
(E) Same as in (D) but for the $Crhr1_{VTA}$ group ($n$ = 17 mice).
(F) Same as in (E) but for the $Crhr1_{VTA}$ group ($n$ = 17 mice).
(G) Same as in (D) but for the $Vgat_{VTA}$ group ($n$ = 8 mice).
(H) Same as in (E) but for the $Vgat_{VTA}$ group ($n$ = 8 mice).
(I) *Z* scored GCaMP fluorescence from recordings aligned to lever press bout onset and separated by bouts occurring prior to (lighter shade) and after (darker shade) 50% of all completed reinforcement ratios for the $Cck_{VTA}$ group ($n$ = 17 mice).
(J) Same as in (J) but for the $Crhr1_{VTA}$ group ($n$ = 17 mice).
(K) Same as in (J) but for the $Vgat_{VTA}$ group ($n$ = 8 mice).
(L) Correlations across bouts between percentage of breakpoint and mean *Z* scored GCaMP signal during bout onset for the $Cck_{VTA}$ group ($n$ = 165 bouts). Correlation coefficient (r) and $p$ values are shown on the top right of the plot.
(M) Same as in (M) but for the $Crhr1_{VTA}$ group ($n$ = 172 bouts).
(N) Same as in (M) but for the $Vgat_{VTA}$ group ($n$ = 172 bouts).
(O) Pearson's correlation coefficient per mouse between percentage of breakpoint and mean *Z* scored GCaMP signal for $Cck_{VTA}$ ($n$ = 17 mice), $Crhr1_{VTA}$ ($n$ = 17 mice), and $Vgat_{VTA}$ ($n$ = 8 mice) groups (see Table S1 for statistical values).

Author Manuscript Author Manuscript Author Manuscript Author Manuscript

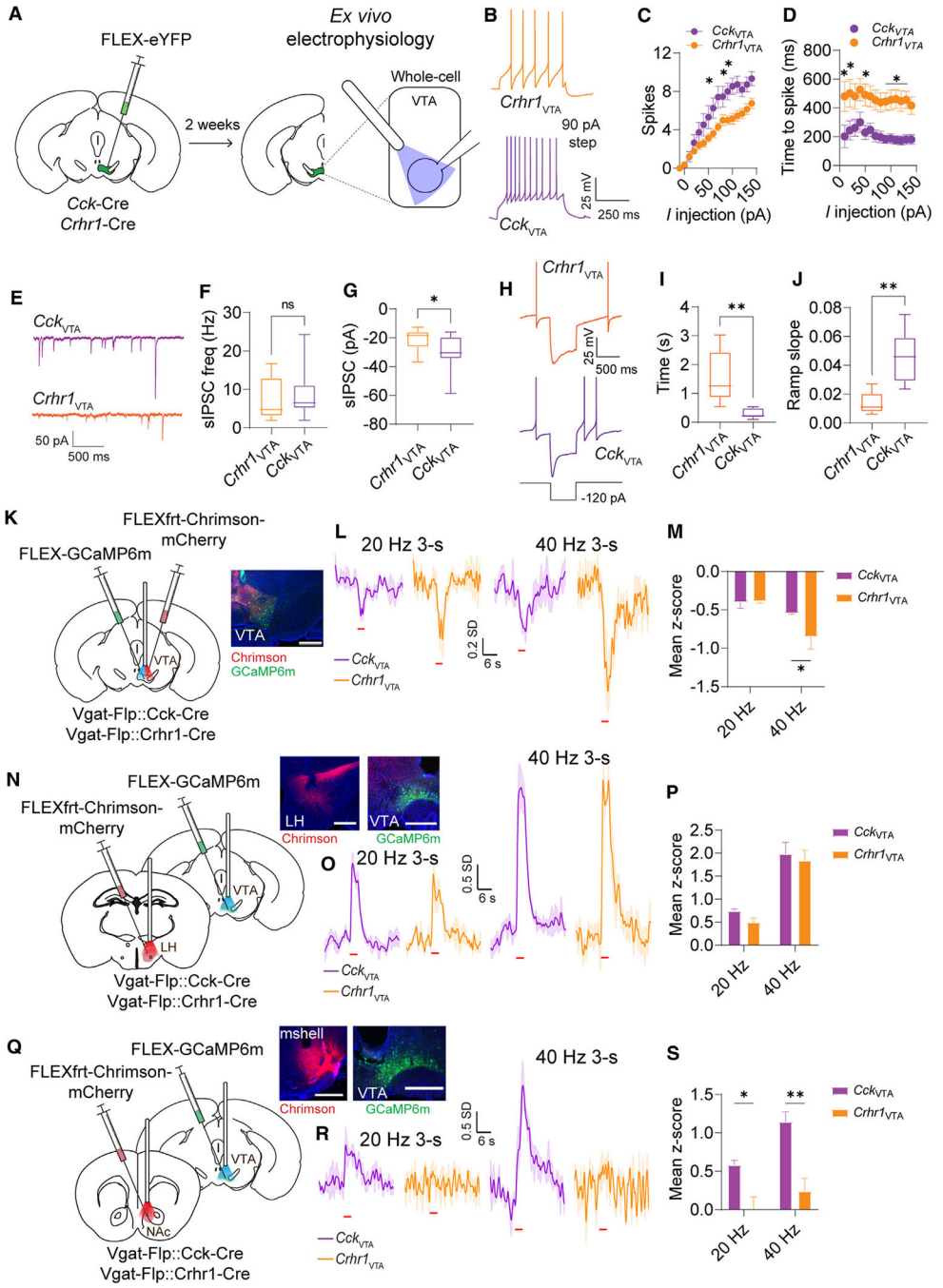


**Figure 6. Properties and connectivity of *Crhr1*$_{VTA}$ and *Cck*$_{VTA}$ neurons**

(A) Schematic of the viral injection strategy and *ex vivo* electrophysiology recordings.

(B) Representative evoked excitability traces (90 pA current injection).

(C) Current-voltage plot for *Crhr1*$_{VTA}$ and *Cck*$_{VTA}$ neurons ($n$ = 13–15 cells). Bars and error bars indicate mean ± SEM across cells.

(D) Mean spike latency following current injection for *Crhr1*$_{VTA}$ and *Cck*$_{VTA}$ neurons ($n$ = 13–15). Bars and error bars indicate mean ± SEM across cells.

Author Manuscript Author Manuscript Author Manuscript Author Manuscript

(E) Representative spontaneous inhibitory postsynaptic current (sIPSC) traces from *Crhr1*$_{VTA}$ or *Cck*$_{VTA}$ neurons.
(F) Mean sIPSC frequency for *Crhr1*$_{VTA}$ and *Cck*$_{VTA}$ neurons ($n$ = 13–15 cells).
(G) Mean sIPSC amplitude for *Crhr1*$_{VTA}$ and *Cck*$_{VTA}$ neurons ($n$ = 13–15 cells).
(H) Representative traces of rebound spiking from *Crhr1*$_{VTA}$ or *Cck*$_{VTA}$ neurons following injection of a −120 pA hyperpolarizing current.
(I) Mean time to first spike following hyperpolarization for *Crhr1*$_{VTA}$ and *Cck*$_{VTA}$ neurons ($n$ = 5–6 cell).
(J) Mean ramp slope prior to first spike following hyperpolarization for *Crhr1*$_{VTA}$ and *Cck*$_{VTA}$ neurons ($n$ = 5–6 cells; see Table S1 for statistical values).
(K) Schematic of viral injection strategy for Flp-dependent Chrimson and Cre-dependent GCaMP into the VTA with optical fiber implanted above VTA. Scale bar: 500 μm.
(L) $Z$ scored GCaMP fluorescence aligned to Vgat$_{VTA}$ stimulation in *Cck*$_{VTA}$ and *Crhr1*$_{VTA}$ groups.
(M) Average $Z$ scored GCaMP fluorescence during stimulation and post-stimulation periods from (L). Bars and error bars indicate mean ± SEM across mice.
(N) Schematic of viral injection strategy for expression of Flp-dependent Chrimson into the LH and Cre-dependent GCaMP into the VTA. Stimulation and recording fibers were implanted above the LH and VTA, respectively. Scale bar: 500 μm.
(O) $Z$ scored GCaMP fluorescence aligned to LH GABA stimulation in *Cck*$_{VTA}$ and *Crhr1*$_{VTA}$ groups.
(P) Average $Z$ scored GCaMP fluorescence during stimulation and post-stimulation periods from (O) for *Cck*$_{VTA}$ ($n$ = 5 mice, 10 sessions) and *Crhr1*$_{VTA}$ ($n$ = 3 mice, 6 sessions) groups (bottom). Bars and error bars indicate mean ± SEM across mice.
(Q) Schematic of viral injection strategy for expression of Flp-dependent Chrimson into the NAc mshell and Cre-dependent GCaMP into the VTA. Stimulation and recording fibers were implanted above the NAc mshell and VTA, respectively. Scale bar: 500 μm.
(R) $Z$ scored GCaMP fluorescence aligned to NAc shell stimulation in *Cck*$_{VTA}$ and *Crhr1*$_{VTA}$ groups.
(S) Average $Z$ scored GCaMP fluorescence during stimulation and post-stimulation periods from (R) for *Cck*$_{VTA}$ ($n$ = 3 mice, 6 sessions) and *Crhr1*$_{VTA}$ ($n$ = 3 mice, 6 sessions) groups (bottom). Bars and error bars indicate mean ± SEM across mice (see Table S1 for statistical values).

Author Manuscript Author Manuscript Author Manuscript Author Manuscript

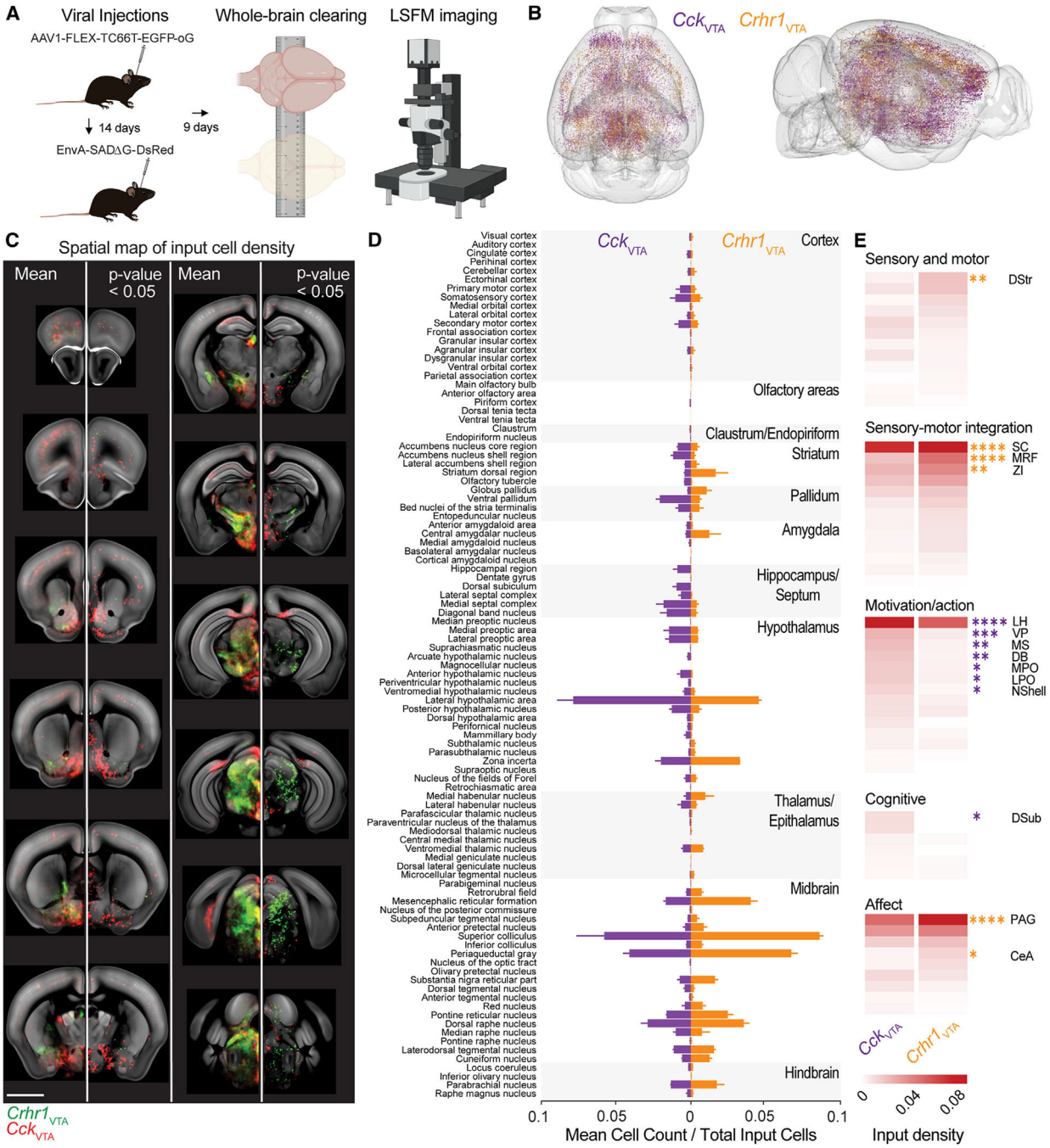


**Figure 7. Whole-brain mapping of inputs to *Crhr1*$_{VTA}$ and *Cck*$_{VTA}$ neurons**

(A) Schematic of viral injection strategy, whole-brain clearing, and light sheet fluorescence microscopy (LSFM). Cre-dependent helper virus (AAV-*syn*-DIO-TC66T-2A-EGFP-2A-oG) was injected, and 2 weeks later, rabies virus (EnvA-SADDG-RV-dsRed) was injected into the VTA. Nine days later, intact brains were cleared and imaged.

(B) Location of input cells to *Cck*$_{VTA}$ and *Crhr1*$_{VTA}$ neurons in example mice.

Author Manuscript Author Manuscript Author Manuscript Author Manuscript

(C) Voxelized heatmap of input cell density in coronal sections across the whole brain. Mean density of dsRed-positive cells per $mm^3$ across mice (left). Voxelized results of group one-way ANOVA pairwise comparison (right) ($n$ = 3 mice). Scale bar: 2 mm.
(D) Mean number of input cells normalized to total number of input cells for all input regions ($n$ = 3 mice/group).
(E) Heatmap of group pairwise comparison one-way ANOVA results for clustered input regions (see Table S1 for statistical values).

Author Manuscript Author Manuscript Author Manuscript Author Manuscript

## KEY RESOURCES TABLE

| REAGENT or RESOURCE | SOURCE | IDENTIFIER |
|---|---|---|
| Antibodies | | |
| anti-tyrosine hydroxylase | EMD Millipore | AB152; RRID:AB_390204 |
| anti-dsRed | Takara | 632496; RRID:AB_10013483 |
| anti-GFP | abcam | ab13970; RRID:AB_300798 |
| Secondary antibodies conjugated with Alexa Fluor 488 or Cy3 | Jackson ImmunoResearch | 703-545-155; RRID:AB_2340375 or 711-165-152; RRID:AB_2307443 |
| Bacterial and virus strains | | |
| AAV1-DIO-ChR2-YFP | University of Washington | N/A |
| AAV1-DIO-JAWS-GFP | University of Washington | N/A |
| AAV1-DIO-GCaMP6m | University of Washington | N/A |
| AAV1-DIO-EGFP-KASH | University of Washington | N/A |
| AAV1-DIO-YFP | University of Washington | N/A |
| AAV-*syn*-DIO-TC66T-2A-eGFP-2A-oG | University of Washington | N/A |
| EnvA-SADΔG-RV-DsRed | University of California | N/A |
| AAV1-CAG-FlpX-ChrimsonR-tdTomato | University of Washington | N/A |
| Experimental models: Organisms/strains | | |
| *Slc6a3*$^{Cre/+}$ (DAT-Cre) mice | Jackson laboratory | 006660; RRID:IMSR_JAX:006660 |
| *Cck*$^{Cre/+}$ mice | Jackson laboratory | 012706; RRID:IMSR_JAX:012706 |
| *Slc32a1*$^{Cre/+}$ (Vgat)-Cre mice | Jackson laboratory | 028862; RRID:IMSR_JAX:028862 |
| *Vgat*$^{flp/+}$ | Jackson laboratory | 029591; RRID:IMSR_JAX:029591 |
| *Crhr1*$^{Cre/+}$ | University of Washington | N/A |
| Software and algorithms | | |
| Fiji | Schindelin et al.[82] | N/A |
| CellProfiler 4.1.3 | McQuin et al.[83] | N/A |
| Clampfit | Molecular Devices | N/A |
| Synapse | Tucker-Davis Technologies | N/A |
| MATLAB | The MathWorks, Inc | N/A |
| Python | Python Software Foundation | N/A |
| R | The R Foundation | N/A |
| Med-PC | Med Associates, Inc | N/A |
| Wholebrain | Fürth et al.[84] | N/A |
| SMART | Jin et al.[85] | N/A |
| ClearMap | Kirst et al.; Reneir et al.[69] | N/A |
| Data analysis code (GitHub) | University of Washington | doi.org/10.5281/zenodo.13162055 |